

# A Separation Control CFD Validation Test Case

## Part 2. Zero Efflux Oscillatory Blowing

David Greenblatt,<sup>\*</sup> Keith B. Paschal,<sup>†</sup> Chung-Sheng Yao<sup>‡</sup> and Jerome Harris<sup>§</sup>  
*Flow Physics and Control Branch, NASA Langley Research Center, Hampton VA 23681-2199*

The control of a separated flow over a wall-mounted hump, by means of two-dimensional zero efflux perturbations, was studied experimentally in order to generate a data set for a workshop aimed at validating CFD turbulence models. Part 1 of this paper considered details of the baseline (uncontrolled) case and a steady-suction control case. The data set for a specific zero efflux control case comprised static surface pressures together with phase-averaged dynamic surface pressures and PIV flowfield measurements. Additional static and dynamic surface pressures were acquired for a variety of control amplitudes, control frequencies and Reynolds numbers. Due consideration was given to characterizing the flow in the vicinity of the control slot, with and without external flow, and to perturbation two-dimensionality. Triple-decomposition of the fluctuating velocity and pressure fields was employed for presenting and analyzing the experimental data. This facilitated an assessment of the mechanism of separation control and the quantification of the coherent and turbulent surface pressures, Reynolds stresses and energy fluxes. Spanwise surface pressures and phase-averaged stereoscopic PIV data revealed an effectively two-dimensional flowfield despite highly three-dimensional instantaneous flow structures.

### Nomenclature

$A$	=	projected model area, $s \times c$
$b$	=	model slot width
$c$	=	model chord-length
$C_{Dp}$	=	model form drag coefficient
$C_Q$	=	volumetric flux coefficient, $U_s b / U_\infty c$
$C_p$	=	time-mean pressure coefficient
$C_\mu$	=	either steady flow momentum coefficient, $\rho_j U_j^2 b / (\frac{1}{2} \rho_\infty U_\infty^2 c)$ or oscillatory flow momentum coefficient, $2b \overline{u_j^2} / (c U_\infty^2)$
$f_e$	=	excitation frequency
$F^+$	=	reduced excitation frequency, $f_e X_R / U_\infty$
$g$	=	any fluctuating quantity
$h$	=	model height
$H$	=	distance between model base and tunnel ceiling
$M$	=	Mach number
$N$	=	number of PIV image pairs
$P, \tilde{p}, p'$	=	time-mean, coherent and turbulent surface pressure
$q$	=	free-stream dynamic pressure
$\underline{Q}$	=	suction flow rate
$Re$	=	Reynolds number based on model chord-length
$Re_\theta$	=	Reynolds number based on momentum thickness

<sup>\*</sup> NRC Research Associate, Flow Physics & Control Branch, Mail Stop 170, Senior Member.

<sup>†</sup> Aerospace Engineer, Flow Physics & Control Branch, Mail Stop 170, Member.

<sup>‡</sup> Aerospace Engineer, Flow Physics & Control Branch, Mail Stop 170.

<sup>§</sup> Optical Engineering Technician, Flow Physics & Control Branch, Mail Stop 170.

$T$	= duration over which data were acquired
$u', v', w'$	= turbulent velocity fluctuations in directions $x, y, z$ ; also $u'_i, i=1,2,3$
$\tilde{u}, \tilde{v}, \tilde{w}$	= coherent velocity fluctuations in directions $x, y, z$ ; also $\tilde{u}_i, i=1,2,3$
$u_j$	= slot velocity
$U, V, W$	= time-mean velocities in directions $x, y, z$ ; also $U_i, i=1,2,3$
$U_P$	= slot peak blowing velocity
$U_S$	= slot suction velocity
$U_\infty$	= free-stream velocity
$x, y, z$	= coordinate directions measured from the model leading edge
$s$	= model span
$T$	= time over which time-averaging is performed
$X_R$	= distance from the slot to flow reattachment
$\rho$	= air density
$\theta$	= boundary layer momentum thickness
$\langle \rangle$	= denotes phase-averaging
*	= denotes root mean square

## I. Introduction

Separation control by means of zero efflux (zero mass-flux) oscillatory jets is known to be effective in a wide variety of flows under different flow conditions.<sup>1</sup> Control is particularly effective when the perturbations are introduced in a two-dimensional manner, for example, at the leading-edge of a wing or at the shoulder of a deflected flap. It is believed that large spanwise structures in the flow are responsible for momentum transfer across the boundary layer and, in so doing, delay separation. Despite intuitive understanding of the flow, at present there is no accepted theoretical model that can adequately explain or describe the observed effects of the leading parameters such as reduced frequency and momentum input. This difficulty stems partly from the turbulent nature of the flow combined with superimposed coherent structures, which are usually driven by at least one instability mechanism. Due to the increased technological importance of these flows, there is an urgent need to develop turbulence models with a predictive capability. Present attempts to develop such models are hampered in one way or another by incomplete data sets, uncertain or undocumented inflow and boundary conditions, or inadequate flowfield measurements.

This paper is the second part of a low-speed experimental investigation aimed at studying the control of a separated flow region formed over the ramp of a wall-mounted hump model. The original model geometry was designed by Seifert & Pack and tested under cryogenic conditions for a wide range of Reynolds numbers, Mach numbers and control conditions.<sup>2,3</sup> Both parts of the present investigation formed part of a CFD validation workshop sponsored by NASA LaRC, in association with the U.S. Air Force Office of Scientific Research (AFOSR), the European Research Community On Flow, Turbulence And Combustion (ERCOFTAC), the International Association of Hydraulic Engineering and Research (IAHR), QNET-CFD, and the National Institute of Aerospace (NIA). The present case was referred to as “Case 3” of the workshop (see [cfdval2004.larc.nasa.gov/case3.html](http://cfdval2004.larc.nasa.gov/case3.html)) and a summary of some pertinent computations can be found in Rumsey *et al.*<sup>4</sup>

The first part of this paper,<sup>5</sup> (presented at the 2<sup>nd</sup> AIAA Flow Control Conference in Portland, OR, 2004) considered the baseline case and separation control by means of steady suction. This paper considered aspects related to separation control via zero efflux oscillatory blowing. As in the companion paper, a “control test case” was selected and this was subjected to detailed steady and unsteady pressure and flowfield measurements. Additional surface pressure data were acquired at various control reduced frequencies and amplitudes, and Reynolds numbers.

## II. Layout & Scope

This paper continues with a brief review of the experimental setup and discusses the range of measurements and criteria motivating the control test case selection (§III). This is followed by a discussion of the slot calibration and how this is used to quantify the zero efflux boundary condition (§IV). The main section of this paper (§V) provides a framework for decomposing the velocity and pressure fields and subsequent presentation of the data. As a CFD test case, the discussion is geared mainly towards consistency and reliability, rather than detailed analysis of the data. Nevertheless, consideration is given to seemingly anomalous aspects of control; effects of Reynolds number;

reduced frequency; reduced amplitude; generation and formation of the controlling (large coherent structures) LCSs; surface pressure waves; coherent and turbulent flowfield statistics, and two-dimensionality.

### III. Experimental Setup

A full description of the experimental setup is provided in Greenblatt *et al*<sup>5</sup> and thus only a pertinent summary is presented here. The setup consisted of a wall-mounted body (Modified Glauert Hump; height  $h$  and chord-length  $c$ ), located between two glass endplates where the leading and trailing edges were faired smoothly with a wind tunnel splitter plate (see fig. 1). This assembly was installed in an open-return atmospheric wind tunnel where zero efflux separation control was effected by means of a slot located at the 65% chord station on the model. Uncontrolled flow accelerated over the hump forebody and separated over an aft ramp. Both “uncontrolled” (baseline) and “controlled” scenarios were considered under various conditions for  $Re \leq 1,114,800$  and  $M \leq 0.12$ . The model was equipped with 165 streamwise and spanwise static pressure ports and 20 dynamic pressure ports in the separated flow region. In addition to the unsteady pressure ports in the separated region, unsteady pressure measurements were made within the throat of the slot and on the downstream slot edge (see fig. 2). The former was used as an aid in quantifying the control “delivery rms pressure” (see §IV below); the latter was used to establish a fluctuating pressure boundary condition that was used for comparing and analyzing downstream unsteady pressure data (see §V below).

Separation control was achieved using zero efflux oscillatory blowing introduced from the spanwise slot, where careful attention was paid to maintaining slot two-dimensionality. This was achieved by means of a rigid piston, spanning the model, that was secured to the base of the plenum by means of a flexible membrane (fig. 2). The piston was driven externally by six voice-coil-based actuator modules [ATEAM (Aero and Thermally Engineered Actuator Modules) actuators designed and manufactured by J. Kiedaisch, H. Nagib and their associates from IIT], providing maximum slot velocities of approximately 80m/s at frequencies ranging from 60Hz to 500Hz. A view of the assembly from the underside of the model, with three modules removed for purposes of illustrating the piston and membrane, is shown in fig. 3. A photograph of the underside of the model, prior to tunnel installation, is shown in fig. 4. The slot-flow was calibrated and characterized for both tunnel flow-off (quiescent) and flow-on (non-quiescent) conditions, using hot-wire anemometry, throat dynamic pressure measurements and two-dimensional PIV (see §IV and §V below). Replacing the suction manifold used in ref. 5 with the zero efflux actuator used here resulted in a reduction of approximately 20% an inflow boundary layer height  $\delta$  and  $Re_\theta$ . This had a negligible effect on the baseline surface pressures and flowfield.

For purposes of CFD validation, a single test case was selected ( $U_p=26.6\text{m/s}$ ;  $f_e=138.5\text{Hz}$ ) and detailed phase-dependent flowfield measurements were made using two-dimensional and stereoscopic particle image velocimetry (PIV). The specific test case conditions (namely control frequency and amplitude) were selected based on the following three criteria: (1) the peak slot velocity should be of a similar magnitude to the suction slot velocity studied previously;<sup>5</sup> (2) perturbations should exert substantial, but not excessive, control of the separated region; and (3) dimensionless control parameters should correspond to a specific case already tested under cryogenic conditions. The rationale behind these criteria was to (1) facilitate a comparison of the different control schemes; (2) avoid a fully attached flow on the ramp that is less challenging for CFD; and (3) allow a direct comparison with high Reynolds number (cryogenic) conditions. In addition to the test case, surface static and dynamic pressure measurements were made for a wide variety of control frequencies and amplitudes. Furthermore, a comparison of this data set with the cryogenic data set<sup>2,3</sup> provides a unique opportunity to assess the effect of Reynolds number (laboratory versus simulated flight conditions) on control, without the usual complicating effects of transition and compressibility.

For the baseline case and the control test case, two-dimensional PIV measurements were made in the four regions shown in fig. 5. For the control test case, data were acquired and averaged at 36 phases of the control cycle. The selection of these regions was based on acquiring (a) high-resolution measurements in the near vicinity of the control slot (zone 1); and (b) flowfield data over the entire separated region (zones 2-4). Separate phase-resolved stereoscopic PIV data were acquired in planes perpendicular to the zones shown in fig. 5, located at  $x/c=0.7$  and 1.0, corresponding to the spanwise region:  $-0.12 < z/s < 0.12$  ( $z/s = \pm 0.5$  denoted the endplate locations).

### IV. Zero efflux Boundary Condition: Slot Calibration

#### A. Background

A boundary condition for CFD validation that can reliably be considered to be two-dimensional presents a number of challenges, even when using an unquestionably zero efflux device. Firstly, verifying the fidelity of a

device (i.e.  $Q=0$ ) at a specific spanwise location via direct measurement is extremely difficult. Rapid oscillatory changes in flow direction, high instantaneous shear, zero-crossing and near-wall complications introduce unacceptably high uncertainties to both hot-wire and optical measurement techniques.

Secondly, a zero mass-flux device presents a problem when one attempts to quantify it in the sense of a meaningful boundary condition, particularly when comparisons are made with steady blowing or suction. This difficulty stems from the duality of the device in the context of a traditional boundary condition: two-dimensional *steady* blowing is characterized by a momentum coefficient (Poisson-Quinton and Lepage<sup>6</sup>):\*

$$C_\mu = \frac{\rho_J u_J^2 b}{\frac{1}{2} \rho_\infty U_\infty^2 c} \quad (1)$$

but steady slot-suction is quantified by means of a volumetric flux coefficient:

$$C_Q = \frac{Q}{U_\infty L} = \frac{U_S b}{U_\infty c} \quad (2)$$

where  $b$  is the slot width and the subscripts  $J$  and  $S$  refer to “blowing jet” and “suction slot” conditions respectively. The former was demonstrated empirically<sup>6</sup> while the latter appears to have been borrowed from the analysis of homogeneous suction on a flap plate.<sup>7</sup> For unsteady slot-flows, a common approach is to extend the standard momentum coefficient definition to include an oscillatory component:  $u_J = U_J + \tilde{u}_J$ .<sup>1</sup> For a zero efflux incompressible slot-flow (oscillatory blowing and suction:  $C_Q=0$ ), the time-mean momentum coefficient can be written as:

$$C_\mu = \frac{2b}{c} \frac{\overline{\tilde{u}_J^2}}{U_\infty^2} \quad (3)$$

from eqn. (1). This implicitly *assumes* that blowing and suction cycles introduce equal momentum to the flow. This may have some validity when the suction slot velocity  $\tilde{u}_J < U_\infty$ , but cannot be considered universally valid. It may be meaningful to use a combined coefficient ( $C_\mu$ ,  $C_Q$ ), defined during the blowing and suction cycles respectively, which could also be extended to non-zero efflux.

Finally, the generally accepted experimental approach to slot-flow characterization is to calibrate the slot in a quiescent environment, i.e. with  $U_\infty=0$  (tunnel-off) and then *assume* that this calibration remains valid under test conditions ( $U_\infty \neq 0$ ) where the pressure and flowfield data are acquired. It was deemed necessary to directly establish the validity of this assumption.

In summary, the combination of CFD requirements<sup>8</sup> and experimental limitations dictated that the boundary condition should have the properties:

1. It should be substantially two-dimensional along the model span thus implicitly validating the assumption of local  $Q=0$ ;
2. It should be representative of the momentum added during the blowing cycle; and
3. It should be representative of the slot conditions prevailing at  $U_\infty \neq 0$ .

These requirements were fulfilled by the following means:

1. An actuator was designed with the objective of maximizing slot-flow two-dimensionality.
2. Slot velocities were measured at multiple spanwise locations.
3. Slot velocities were measured for both  $U_\infty = 0$  and  $U_\infty \neq 0$ .
4. Simultaneous unsteady pressure fluctuations were measured in the throat of the slot for both  $U_\infty=0$  and  $U_\infty \neq 0$ .
5. 2-D phase-averaged PIV measurements were made within, and in the near vicinity of, the slot at the test condition ( $U_\infty=34.6\text{m/s}$ ).

With the above requirements as a guideline, we proceed to discuss the calibration methods and results below.

## B. Quiescent Environment Calibration

The near field of a steady two-dimensional jet consists of a laminar (or potential) core often termed a “top-hat” profile. On the other hand, steady suction through a slot produces a sink-flow in its near vicinity.<sup>9</sup> In zero efflux

---

\* The active flow control *momentum coefficient* ( $C_\mu$ ) should not be confused with the *closure coefficient* commonly used in turbulence models.

oscillatory jets, the velocity profiles develop in a spatial and temporal manner, but the peak blowing velocity associated with a cycle is seen to be associated with a similar type of top-hat profile. Fig. 6a shows phase-averaged hot-wire data acquired in the slot that is divided into blowing and suction cycles. (Note that  $\phi=0^\circ$  is shifted by  $80^\circ$  from that posted at [cfdval2004.larc.nasa.gov/case3.html](http://cfdval2004.larc.nasa.gov/case3.html)). The coordinate system  $\xi$ - $\psi$  is shown on the figure;  $\psi=0$  is midway between the lower corner of the upper slot edge and the lower slot edge. Within the slot (approximately  $\xi<1$ ), the probe interferes with the flow and this data cannot be relied upon. As the probe traverses out of the slot ( $\xi>1$ ) and its interference of the flow is minimized, the blowing peaks tend towards a constant value at the same phase while the suction peaks diminish. Plotting only the peak values shows that during the blowing cycle, the peak values ( $U_p$ ) are virtually constant for  $1.25<\xi<2.25$ , while the suction peaks exhibit behavior similar to that of a sink flow (fig. 6b). Due to the sink-flow nature of the suction phase, these data have little value in the context of a slot calibration. For CFD boundary condition requirements, all slot calibrations were based on the phase-averaged blowing peak velocities at the point where  $\psi=0$  intersects the virtual surface of the model.  $U_p$  was also found to be insensitive to small vertical changes ( $\Delta\psi = \pm 50\mu\text{m}$ ; hatched section in fig. 6b).

The nature of the peak velocities described here was shown to be similar for different frequencies and amplitudes tested. In addition, unsteady throat pressures were recorded simultaneously. A summary of the throat delivery rms pressure  $p^* = \sqrt{\bar{p}^2}$  versus  $U_p$  is shown in fig. 7 and indicates a useful Bernoulli-type relationship:

$$h \frac{1}{2} \rho U_p^2 = h k p^* \quad (k=1.31) \quad (4)$$

for a wide range of frequencies.

### C. Perturbation Two-Dimensionality

The identification of a core region with approximately constant peak velocity allowed convenient examination of the slot two-dimensionality. This was conducted at three locations on either side of the model centerline covering approximately the central 50% of the model, for  $f_e=138.5\text{Hz}$  and five different throat rms pressures  $p^*$  (fig. 8a). The blowing peaks are shown to be approximately constant along the span, although the peak velocities at  $y/s>0$  appear to be larger for those at  $y/s<0$ . The main reason for this is the non-uniformity of the spanwise slot width  $b$  that varies from 0.79mm to 0.74mm. If we account for this and plot  $bU_p$  (i.e. peak  $Q/s$ ), the asymmetry is effectively eliminated (fig. 8b). It should be noted, however, that the slot non-uniformity results in a small momentum boundary condition asymmetry (fig. 8c). Small effects of the slot non-uniformity were also evident in the cases involving steady suction, where the pressure recoveries were slightly larger for  $y/s<0.5$  (see part 1 of this paper).

### D. Non-Quiescent Calibration Correction

To assess the effect of free-stream velocity on the application of the boundary condition, two approaches were adopted. The first was to conduct hot-wire measurements in the core region of the slot and the second involved high-resolution phase-averaged PIV measurements in the vicinity of the slot. The former is discussed here and the latter is discussed in section IV.

Figs. 9a and 9b show the phase-averaged slot throat pressure and hot-wire measurement for various wind tunnel velocities. With the free-stream velocity, in general both the  $p^*$  and  $U_p$  increase due to broadband vortex shedding. This has the effect of modifying the constant of proportionality. To quantify this, we plot  $\frac{1}{2} \rho U_p^2 / k p^*$  as a function of free-stream velocity, which provides a correction to proportionality constant  $k_c \approx 1.09$ . In order to quantify the CFD boundary condition in dimensionless terms and allow comparison with other investigations, it was assumed that  $\bar{u}_j^2 = U_p^2 / 2$  (i.e. a purely sinusoidal oscillatory flow) and thus from equations (3) and (4):

$$C_\mu = \frac{b k k_c p^*}{c q_\infty} \quad (5)$$

where  $p^*$  data were acquired simultaneously with surface pressure and flowfield data. The test case and vast majority of experiments were performed using  $k_c \approx 1.09$ , but selected data were acquired with  $k_c = 1$  to assess the validity of this widely used assumption. The dimensionless control frequency was expressed as

$$F^+ = \frac{f_e X_R}{U_\infty} \quad (6)$$

where  $X_R$  is the distance from the slot to the baseline reattachment line.

## V. Pressure and Flowfield Data

### A. The Triple Decomposition

For the purposes of presenting and analyzing the experimental data, all fluctuating quantities  $g(x,t)$  were decomposed according to the so-called triple decomposition (Hussain & Reynolds<sup>10,11</sup>):

$$g(x,t) = G(x) + \tilde{g}(x,t) + g'(x,t) \quad (7)$$

where

$$G(x) = \lim_{T \rightarrow \infty} \frac{1}{T} \int_0^T g(x,t) dt, \quad (8)$$

$\tilde{g}(x,t)$  is the purely periodic component and  $g'(x,t)$  is the random turbulence. Experimental data were generally acquired by means of phase averaging:

$$\langle g(x,t) \rangle = \lim_{N \rightarrow \infty} \sum_{n=1}^N g(x,t+n\tau) \quad (9)$$

where

$$\tilde{g}(x,t) = \langle g(x,t) \rangle - G(x) \quad (10)$$

and thus

$$g(x,t) = \langle g(x,t) \rangle + g'(x,t) \quad (11)$$

The triple decomposition aids in understanding the interaction between the coherent and incoherent components of the flowfield and facilitates quantification of the energy fluxes between the mean, coherent and random fields.<sup>12</sup> For the static dynamic pressure data:  $TU_\infty/c = 5000$ ; for the two-dimensional and stereoscopic PIV data:  $400 \leq N \leq 2000$ . In this paper, the subscripts ( $i,j,k$ ) refer to directions ( $x,y,z$ ). For convenience, both subscripted and non-subscripted notations are used.

### B. Pressure & Flowfield Data

Time-mean and rms pressure coefficients for the baseline and test condition are shown in fig. 11a for all measurement locations; corresponding baseline and control time-mean  $U(x,y)$  contours are shown in figs. 11b and 11c respectively. Data at the test condition ( $U_p=26.6\text{m/s}$ ,  $f_e=138.5\text{Hz}$ ) are shown here in dimensionless form ( $C_\mu=0.110\%$ ,  $F^+=0.77$ ) according to eqns. 5 and 6. For the baseline case, separation and reattachment were seen to occur at  $x/c \approx 0.67$  (fig. 13e) and  $x/c \approx 1.105$  (fig. 11b) respectively. Unlike the steady suction case, zero efflux control results in a relatively small effect on the pressure immediately upstream of the slot. Downstream of the slot, the separation point is not significantly affected (also see PIV data below) but the pressure in the vicinity of separation reduces. Just downstream of separation, there is a relatively sharp pressure drop, followed by a pressure recovery that crosses over the baseline with reattachment occurring further upstream. This results in a curious situation where control appears to promote separation close to the control location while simultaneously shortening the reattachment length. This is consistent with high Reynolds number observations made by Seifert & Pack,<sup>2</sup> but at much reduced  $C_\mu$ .

For the control case, periodic and turbulent rms pressure fluctuations

$$C_{\tilde{p}}^* = \sqrt{\tilde{p}^2} / \frac{1}{2} \rho U_\infty^2 \quad \text{and} \quad C_{p'}^* = \sqrt{p'^2} / \frac{1}{2} \rho U_\infty^2$$

are shown as per the definitions in eqn. (7) above. In the context of CFD validation utilizing URANS-type approaches,  $C_{\tilde{p}}^*$  can be directly compared with computed pressure fluctuations. Over the separated region, the turbulent pressure fluctuations associated with control are significantly larger than those of the baseline case. It is interesting to note that fluctuating turbulence peaks occur slightly upstream of reattachment for both the baseline ( $x/c=1.11$ ; cf. fig. 11b) and control ( $x/c=0.98$ ; cf. fig. 11c) cases, in spite of the superimposed coherent motion present in the latter. In the immediate vicinity downstream of the slot,  $C_{\tilde{p}}^*$  far exceeds  $C_{p'}^*$  and this is consistent with greater coherence relative to turbulence associated with the traveling pressure wave. The coherent fluctuations peak in the vicinity of  $C_{P,\min}$  and then decay rapidly and approximately linearly, where the contributions of the coherent and turbulent fluctuations are equal at  $x/c \approx 0.9$ . Thus, the region in which separation is *promoted* is

associated with amplification of the coherent pressure wave; the region of pressure recovery is associated with its dissipation.

Further insight into the time-mean nature of control described above can be obtained by comparing velocity profiles  $U(x)$  in the separated region (figs. 12a-12d), where the zero efflux controlled profiles were obtained by time-averaging the 36 phase-averaged profiles. Downstream of the slot at  $x/c=0.75$  (fig. 12a), control increases the momentum in the outer part of the shear layer (discussed further below), but the reverse flow velocities near the wall increase substantially, thereby generating a shallower but stronger recirculation region (or bubble). With increasing  $x/c$  this recirculation region strengthens, as can be seen by the increasing disparity between the outer layer and inner layer profiles (fig. 12b), and this is consistent with the decreasing mean pressure that attains its minimum at  $x/c \approx 0.78$ . Downstream of the pressure minimum, the controlled reverse flow region begins to diminish, while simultaneously the baseline reverse flow region increases such that at  $x/c=0.85$  (fig. 12c) their reverse flow regions are approximately the same. This corresponds approximately to the pressure crossover at  $x/c=0.83$  shown in fig. 11. Further downstream, the larger pressure recovery rate associated with the controlled case (fig. 11) is consistent with the rapidly attaching boundary layer (fig. 12d).

The time-mean behavior described above can be further elucidated with respect to phase-averaged measurements in the near vicinity of the slot (selected phases are shown in figs. 13a-d; normalized vectors (flow direction) are plotted together with contours of the  $U$ -component of velocity). At the transition between the blowing and suction phases ( $\phi=0^\circ$ ), the shear layer pulled relatively close to the model surface upstream of the slot (fig. 13a). On the ramp downstream of the slot, the separation point can also be discerned at  $x/c \approx 0.677$ . As the slot blowing amplitude increases, the separation point progresses up the ramp and at the phase corresponding to the blowing peak, separation has progressed to  $x/c \approx 0.664$  with the shear layer deflected away from the wall (fig. 13b). The velocity vectors between the slot and separation point are pointing away from the wall and the velocity upstream of the slot is retarded. As the blowing amplitude diminishes, upstream velocity remains retarded and the separation point does not move significantly, although the near-wall velocities increase. With the commencement of the suction phase, the separation point moves rapidly downstream and halfway through the suction cycle, the separation point has moved out of the field of view shown here ( $x/c > 0.68$ ), velocity vectors are tangent to the ramp wall and high velocity flow is established upstream of the slot.

These measurements illustrate to some degree the mechanism behind the time-mean observations discussed with respect to zero efflux control above: the blowing and suction phases tends to alternately promote and reduce separation close to the slot respectively. In a similar fashion, the near-wall velocity upstream of the slot alternately increases and decreases depending on the phase. This accounts for the lack of a “suction peak” upstream of the slot such as that observed when control is applied by means of steady suction alone. Although the detrimental effect during the blowing cycle may seem counterintuitive, there is a precedent in the application of boundary layer control (BLC) by steady blowing (see fig. 1 of Attinello<sup>13</sup>). When steady control is applied upstream of separation with  $u_j/U_\infty \leq 1$  the jet serves to retard the boundary layer flow resulting in lower near-wall momentum and hence a boundary layer that is more susceptible to separation. A threshold slot velocity ratio  $u_j/U_\infty \sim 1$  must be reached before a positive net effect, such as an increase in lift, is observed. Kelly *et al* (see Attinello<sup>13</sup>), proposed a steady blowing net momentum coefficient:

$$C_{\mu,net} = (1 - U_\infty/U_j) \times C_\mu \equiv C_\mu - 2C_Q \quad (12)$$

which correlated well with airfoil data. In this zero efflux control experiment, as well as some others, a similar mechanism may be at work. For example, in many low-speed investigations, model or airfoil slot width to chord ratios are within the range:  $0.1\% < b/c < 0.3\%$ . From the definition shown in eqn 3, this corresponds to the same  $C_\mu$  range when  $U_P/U_\infty = 1$ . Support for this suggestion can be found from many investigations that cite a threshold  $C_\mu$  in this range above which zero efflux separation control becomes effective.<sup>1</sup> Using a similar argument to that presented in Attinello<sup>13</sup> above, we can express a net zero efflux momentum coefficient as:

$$C_{\mu,net} = (1 - U_\infty/U_P) \times C_\mu \equiv C_\mu - \sqrt{2}C_{QP} \quad (13)$$

where  $C_{QP} = bU_P/cU_\infty$ . Care should be exercised when applying eqn. 13 to a zero efflux case because in many instances substantial performance enhancements are observed with  $C_{\mu,net} < 0$ ! This is because, unlike steady BLC, the shear layer instability and subsequent rollup of large coherent structures (LCSs) play a dominant role in determining the separation control attributes (see data and discussion below). Note that an argument can be made for the superposition of a net positive<sup>14</sup> or negative<sup>1,2</sup> mass-flux to enhance separation control effectiveness: when the overall jet peak velocity exceeds  $U_\infty$ , the blowing phase results in a net increase in near-wall momentum but the

shear layer may be more stable; when the overall jet peak velocity is zero, no low momentum fluid is introduced and the shear layer may be more unstable.

### C. Effect of Reynolds Number, Control Frequency and Control Amplitude

The mean and oscillatory pressure data described above were found to be almost completely independent of Reynolds number for the range considered here (figs. 14a and 14b). Note that each control case required a different physical frequency and amplitude to achieve the same reduced conditions (see §IV and figs. 5-10 for details). Although the Reynolds number range presented here is small, a larger effect was discerned with respect to steady suction data for the same  $Re$  range (see part 1 of this paper).<sup>5</sup> Like part 1 of this paper, the present setup together with the cryogenic setup of Seifert & Pack facilitated a unique ability to assess the effect of Reynolds number without the usual complications associated with transition and compressibility. A comparison at the test condition (fig. 16) shows a dramatic difference in the effectiveness of control at the different Reynolds numbers. To better understand this effect we show the steady suction comparison for  $C_{Dp}$  (fig. 17a) for atmospheric and cryogenic conditions (not shown in part 1 of this paper). Both data sets have a linear range where  $C_{Dp} \propto -C_\mu$ . Note, however, that  $-dC_{Dp}/dC_\mu$  increases by an order of magnitude when the Reynolds number is increased by a factor of 16. It is believed that minor differences in slot geometry between the two models, discussed in ref. 5, play only a secondary role. Consistent with the present zero efflux data, a much smaller Reynolds number effect is evident for a 16 times increase (fig. 17b). A further explanation for the present small  $Re$  effect is discussed below with respect to saturation of control authority.

Slot calibration for quiescent ( $k_c=1$ ) and non-quiescent ( $k_c=1.09$ ) conditions was assessed for the test case in fig. 15. For this case the differences are negligible and it might be concluded that a quiescent calibration is sufficiently representative. It will be shown below, however, that the control authority saturates and thus this conclusion may not be universally valid.

The effect of increasing the excitation amplitude at the test case frequency can be seen in figs. 18a-18d. Based on these data, separation control can be characterized differently for “low” and “high”  $C_\mu$  respectively as explained below. For low  $C_\mu$ , excitation reduces the overall bubble length, as can be seen from the pressure recovery, but the reverse flow region (bubble) downstream of the slot increases as is evidenced by the level and location of the low pressure region. This process of strengthening and shortening the bubble continues with increasing  $C_\mu$ , but saturates at  $C_\mu \approx 0.11\%$ , which coincidentally corresponds to the test case discussed above. The relative insensitivity to  $C_\mu$  in this range may also be responsible for masking Reynolds number effects (see fig. 14a). Increasing  $C_\mu$  is accompanied by increases in coherent and random pressure fluctuations (figs 18c and 18d), which typically achieve their peak values closer to the slot as  $C_\mu$  increases. For  $C_\mu$  approximately greater than 0.11%, forcing begins to diminish the strength of the bubble as the pressure just downstream of the slot begins to recover and the overall bubble-length continues to shorten. In addition,  $C_p^*$  and  $C_p^{*}$  saturate and their amplitudes decrease relative to the fluctuation amplitudes at the lower lip of the slot (left-most data points), which we consider to be the fluctuating pressure “boundary conditions” (see §III and fig. 2). The amplitude range at which these observations are made, namely cessation of bubble mean pressure reduction and suppression of pressure amplification, may be considered to be a transition range approximately demarcating low and high amplitude control. The surface pressure fluctuations are proportional to the strength of the spanwise momentum-transferring vortices (see figs. 21a-21f below) and thus it may be conjectured that the low amplitude perturbations (approximately  $C_\mu < 0.11\%$ ) rely predominantly on excitation of the free shear layer to effect separation control. With high-amplitude control, separation control relies more on alternately adding momentum via blowing and removing the boundary during the suction, and it is less clear how much high amplitude forcing of the shear layer contributes. Similar observations were made at various reduced frequencies in the range  $0.45 \leq F^+ \leq 1.94$ . In the present case, a pressure recovery immediately downstream of the slot is only evident when  $C_\mu \approx 0.35\%$ , but this value is somewhat dependent on  $F^+$  as will be shown below. The asymmetry associated with the pressure recovery (fig. 18b) over the central part of the model ( $-0.25 \leq z/s \leq 0.25$ ) is believed to be due to the momentum asymmetry introduced as a result of spanwise slot variation.

The effect of increasing the reduced frequency  $F^+$  at constant  $C_\mu$  is shown in figs. 19a-19d for selected cases. At low control frequencies (approximately  $F^+ < 1$ ) increasing the frequency has a similar effect to that of increasing  $C_\mu$ , namely the near wall reverse flow region intensifies but the reattachment length reduces. A decrease in pressure downstream of the slot is associated with an improved pressure recovery near reattachment. However, an optimum frequency is reached where the shortest pressure recovery occurs at  $1.05 \leq F^+ \leq 1.35$ ; this corresponds approximately to that associated with attaching a separated shear layer to a deflected flap using small  $C_\mu$ .<sup>15</sup> With further increases

in  $F^+$  this mean pressure trend reverses, i.e. pressure drop immediately downstream of the slot is smaller, but the recovery is adversely affected near reattachment. The amplification of the coherent and turbulent wall pressure fluctuations is dramatically affected by changes in frequency. The highest levels of turbulent and coherent pressure fluctuations occur for  $F^+=0.77$  and  $0.45$  respectively (figs. 19c and 19d), which is somewhat less than the optimum for separation control. At frequencies higher than the optimum  $F^+$ , turbulent pressure fluctuations show a net decrease when compared to their value at the lip of the slot. Coherent fluctuations always amplify at some distance downstream of the slot, and with increasing frequency they (a) attain their peak values closer to the slot; (b) dissipate over a successively shorter distance; and (c) respond in an increasingly non-linear fashion. It is evident that the shear layer stability also plays a defining role in the transfer of momentum from the free-stream to the wall. To adequately predict the effect of control, both the slot effect and the shear layer instability must be properly accounted for.

The effect of control amplitude and frequency on  $C_{Dp}$  is summarized in fig. 20; the baseline value is indicated on the ordinate. The process of strengthening and shortening the bubble with increasing amplitude manifests as a form-drag *increase* at low  $C_\mu$ . At higher frequencies, where the bubbles are shorter, the drag increase is smaller. Higher amplitude control achieved at lower Reynolds numbers, resulted in further ramp pressure increases immediately downstream of the slot and a net decrease in  $C_{Dp}$  that was only observed at  $C_\mu$  corresponding to  $U_p/U_\infty > 1$ . Steady suction ( $F^+=0$ ), on the other hand, always increases the ramp pressure as is evident in fig. 20 and is clearly more effective than zero efflux control for reducing drag. However, for control at high amplitudes, there is a crossover  $C_\mu$  where zero efflux control becomes more effective. The comparison shown here should be viewed in the context of the limitations discussed with respect to slot calibration in §IV.

#### D. Mechanism of Control

The generation, rollup and shedding of the vortex for the test case is described with respect to figures 21a-21f, which show the simultaneous phase-averaged spanwise vorticity field ( $\langle \omega_z \rangle = \partial \langle v \rangle / \partial x - \partial \langle u \rangle / \partial y$ ) and the coherent surface pressures  $C_{\bar{p}}$  at six phases. Soon after the start of the blowing phase ( $\phi=30^\circ$ ; fig. 21a) the shear layer downstream of the slot is deflected downward towards the model surface. This feature is an artifact of the suction cycle that preceded the blowing cycle (discussed below with respect to fig. 21f). A previously generated vortex is centered at  $x/c \approx 0.9$  and corresponds approximately to a local pressure minimum. A region of weaker vorticity also exists at  $1.6 < x/c < 2.4$ , corresponding to the additional local pressure minimum, but it cannot be seen on the present scale. The region of high positive vorticity close to the wall is indicative of the extent and magnitude of the near-wall reverse flow region.

As the blowing increases to its peak value ( $\phi=90^\circ$ ; fig. 21b) the shear layer just downstream of the slot lifts off the wall, thereby distorting the layer. The region of reverse flow now exits over virtually the entire ramp commencing at  $x/c \approx 0.664$  (cf. figs. 13d and 21b). This distorted shear layer characterizes the early stages of vortex rollup and is associated with a pressure minimum just downstream of the slot shoulder. At this phase, three distinct pressure minima are present, corresponding approximately to the three vortices existing simultaneously in the measured flowfield. As the blowing amplitude diminishes ( $\phi=150^\circ$ ; fig. 21c), the vortex becomes more pronounced and convects downstream and induces a region of larger positive vorticity (reverse flow) near the wall as a consequence of the no-slip condition. As the control switches from blowing to suction ( $\phi=210^\circ$ ; fig. 21d), the vortex begins to break away from the shear layer. The distinct shear layer and vortex coexisting produce the non-linear pressure response shown in the upstream pressure ports. In the middle of the suction phase ( $\phi=270^\circ$ ; fig. 21e) the shear layer is pulled close to the wall near the slot, resulting in a highly curved shear layer, although the vortex is not fully shed from the shear layer. Toward the end of the suction cycle, the vortex breaks free and convects downstream. The distance between negative pressure peaks is indicative of the spacing between the vortices, and reflects the increasing phase velocity ( $U_\phi$ ) of the vortices as they are generated and convected downstream.

Phase-averaged surface pressures at the test case reduced control frequency ( $F^+=0.77$ ) are shown for increasing control amplitude in figs. 22a-22f (corresponding to fig. 18d), where fig. 22d represents the test case amplitude described with respect to figs. 21a-21f above (cf. mean and rms pressures in figs. 18a-18d). The data at  $x/c=0.65$  represents the slot throat delivery pressure. As expected, there are no appreciable fluctuations in the uncontrolled baseline flow at the test frequency (fig. 22a). For small amplitude excitation (fig. 22b), the pressure fluctuations gradually amplify, with a flat peak around  $x/c=1$ , and then gradually decay. Based on the observation that rolled-up vortices are associated with negative pressure peaks (figs. 21a-21f), we can conclude that there are typically two to three vortices present in the measurement region ( $0.65 \leq x/c \leq 1.4$ ) at any instant. Increasing the control amplitude results in larger pressure fluctuations with peaks gradually becoming more pronounced and closer to the slot (figs.

22c and 22d). Note, however, that the amplification relative to the delivery pressure decreases. For  $C_{\mu} \geq 0.110\%$ , the gross amplification saturates and this corresponds to the lowest mean pressure downstream of the control location (see figs. 18a and 18d). Note, however, that the wave speed of each vortex ( $U_{\phi} = \lambda f_{\phi}$ ) is not significantly changed by the relatively large increase in control amplitude.

Similar data at the test case reduced control amplitude ( $C_{\mu} = 0.110\%$ ) are shown for increasing  $F^+$  in figs. 23a-23f (cf. mean and rms pressures in figs. 19a-19d). At the lowest frequency considered here ( $F^+ = 0.45$ ) the fluctuations amplify close to the slot, maintain their amplitude up to  $x/c \approx 1$ , and gradually decay. In fact, the amplitudes are still significant well downstream of the baseline reattachment point (see also discussion above). Based on pressure minima, there is never more than one vortex present in the separated region at any instant. As expected, increased control frequency brings about increased wave speed and amplification near the slot together with decay commencing closer to the slot and over a shorter distance. At  $F^+ = 1.94$ , the strong non-linear effects mentioned above are further elucidated (fig. 23f; 19d), namely a coherent pressure wave is generated with a wavelength exceeding  $0.75 \leq x/c \leq 1.4$ . The frequencies that bring about the shortest overall pressure recovery ( $1.05 \leq F^+ \leq 1.34$ ) typically have between 2 to 3 vortices present in the separated region at any instant (cf. ref 15).

### E. Coherent and Turbulent Statistics

Phase-averaged coherent and turbulent Reynolds stresses ( $\langle \tilde{u}_i \tilde{u}_j \rangle$  and  $\langle u'_i u'_j \rangle$ ) are shown for the peak-blowing phase ( $\phi = 90^\circ$ ; figs. 24a-c and 24d-f) and at the middle of the suction phase ( $\phi = 270^\circ$ ; figs. 25a-c and 25d-f). The coherent generation and shedding of the separation control vortices produce regions or “islands” of relatively high coherent stresses. The wavelength between typical regions in the downstream direction is approximately half of the wavelength between successive vortices. As expected, the coherent stresses dissipate in the downstream direction. Figs. 24d-f and 25d-f show the extent to which the coherent motion also organizes the turbulent Reynolds stresses into concentrated regions. These correspond approximately to the regions of high vorticity that are associated with the rolled up vortices (see figs. 21b and 21e), where local peak values of  $\langle u'u' \rangle$  exceed  $-\langle u'v' \rangle$  and  $\langle v'v' \rangle$  by a factor of about 2. The stresses involving  $-\langle \tilde{u}\tilde{v} \rangle$  show both negative and positive values (figs. 24c, 25c; note the different scale). The reason for the unusual negative  $-\langle \tilde{u}\tilde{v} \rangle$  is that localized positive  $\tilde{u}$  and  $\tilde{v}$  (during the blowing cycle) and negative  $\tilde{u}$  and  $\tilde{v}$  (during the suction cycle) occur simultaneously. The triple decomposition makes clear that this does not arise from the turbulence supplying energy to the mean flow, but rather the interaction of the coherent oscillations in the flow. It will be noted below (see figs. 26f) that in a time-mean sense the term  $-\langle \tilde{u}\tilde{v} \rangle$  is always positive and small because the net transfer of energy, through the cycle, from the mean to the coherent motion is slightly larger. It is therefore concluded that these features do not arise as a result of so-called vortex nutation<sup>16</sup> where the orientation of the vortex gives rise to a net transfer of energy to the mean flow.

Time averaged data resulting from the triple decomposition is useful for understanding how the perturbations produce and spatially organize the turbulence.<sup>10,11</sup> It also allows comparison of the relative magnitudes and spatial distribution of the coherent and turbulent stresses. The time-averaged baseline turbulent stresses ( $\overline{u'_i u'_j}$ ) and control coherent and turbulent stresses ( $\overline{\tilde{u}_i \tilde{u}_j}$  and  $\overline{u'_i u'_j}$ ) are shown in figs. 26a-c, 26d-f and 26g-i, respectively. As a general rule, the coherent stresses attain their largest values close to excitation slot where the coherent perturbations are most significant. For example, the concentrated  $\overline{\tilde{u}\tilde{u}}$  near the slot and its proximity to the surface (nearly normal to the surface) is mainly responsible for the large  $C_p^*$  on the wall. Although positive values of  $\langle \tilde{u}\tilde{v} \rangle$  are observed at various phases of the control cycle, they do not emerge as a dominant feature in a time-averaged sense. The relatively large turbulent stresses associated with control and their distribution within the flowfield is consistent with the magnitude and distribution of the turbulent pressure fluctuations  $C_p^*$  (e.g. fig. 11). Energy flux from the mean flow to the coherent and turbulent fields (figs. 27a-c):

$$-\overline{\tilde{u}_i \tilde{u}_j} \frac{\partial U_i}{\partial x_j} \quad \text{and} \quad -\overline{u'_i u'_j} \frac{\partial U_i}{\partial x_j}$$

can also be calculated from the mean flow statistics.<sup>10,11</sup> These data clearly show how separation control results in significant coherent energy transfer near the slot, but further downstream this is superseded almost entirely by energy transfer to the turbulent motion. The energy transferred to the turbulence with control moves upstream, intensifies and is brought closer to the ramp consistent with the pressure and flowfield data presented above.

## F. Flowfield Two-Dimensionality

Aspects of the flow two-dimensionality were considered previously from the perspective of the model geometry,<sup>5</sup> slot perturbations (§IV.C.) and spanwise pressures on the ramp (§V.C.). In this section flowfield two-dimensionality was considered by means of stereo PIV measurements, in planes  $x/c=0.7$  (close to the slot) and  $x/c=1.0$  (in the vicinity of time-mean reattachment line) extending over the spanwise distance  $-0.12 \leq z/s \leq 0.12$ . Phase-averaged velocity fields at  $x/c=0.7$  showed effectively two-dimensional flow. Examples of the three instantaneous velocity components ( $u, v, w$ ) near reattachment ( $x/c=1.0$ ) for individual image pairs at a single phase ( $\phi=60^\circ$ ) are shown in figs. 28a-28d. Despite the effectively two-dimensional perturbations, the instantaneous velocity field is highly three-dimensional with instantaneous velocity components of similar magnitude. For the streamwise velocity component, localized reversed flow regions penetrate well into the boundary layer (to approximately the height of the model,  $y/h=1$ ), and in-plane  $\sqrt{v^2 + w^2}$  velocities are as large as  $0.8U_\infty$ . The streamwise vortical structures have a maximum size and spacing that is approximately  $h/2$ . Phase-averaged streamwise velocities ( $\langle u \rangle, \langle v \rangle, \langle w \rangle$ ) for six phases are shown in figs. 29a-29f. It is evident that the highly three-dimensional flow has no preferred time-mean structure. The spanwise variations and cross-stream velocity components are on the order of the error associated with the PIV measurement ( $0.03U_\infty$ ).

Phase-averaged turbulent statistics also indicate flow two-dimensionality as shown in the example of the six Reynolds stress components shown at  $\phi=0^\circ$  (figs. 30a-30f). The relatively large  $\langle u'u' \rangle$  with respect to  $-\langle u'v' \rangle$  and  $\langle v'v' \rangle$  is consistent with the two-dimensional PIV data discussed in (§V.E.). Despite the large instantaneous structures present in the flow (fig. 28),  $w'$  is virtually uncorrelated with either  $u'$  or  $v'$  (figs. 30e and 30f). This might serve as a justification for modeling the flow using a two-dimensional URANS approach.

## VI. Concluding Remarks

This paper summarized the second part of a CFD validation study of separation control over a wall-mounted hump by means of two-dimensional zero efflux perturbations. The main effort was expended in documenting a single control case that comprised static surface pressures together with phase-averaged dynamic surface pressures and PIV flowfield measurements. Due consideration was given to characterizing the flow in the vicinity of the control slot, with and without external flow, and establishing perturbation two-dimensionality. Spanwise surface pressures and phase-averaged stereoscopic PIV data revealed an effectively two-dimensional flowfield despite highly three-dimensional instantaneous flow structures. The test case is expected to be particularly challenging for CFD codes because different, sometimes counteracting, mechanisms dominate the separated flowfield during different parts of the control cycle.

## VII. Acknowledgements

This work was performed while the first author held a National Research Council–NASA Langley Research Center Associateship. The authors wish to thank W. L. Sellers III, M. J. Walsh, A. E. Washburn, N. W. Schaeffler, A. Seifert (Tel Aviv University), L. P. Melton, M. A. Kegerise, C. L. Rumsey, T. B. Gatski, and P. Balakumar for their assistance and many insightful suggestions. Detailed design and construction of the actuator by J. Kiedaisch, H. Nagib and their associates from IIT, contributed immensely to the data quality, two-dimensionality and long-term repeatability of the experimental data. The authors also wish to thank R. L. Clark, R. S. Geouge, T. E. Fowler and M. Bell for their excellent technical support.

## VIII. References

1. Greenblatt, D. and Wagnanski, I., "Control of separation by periodic excitation", Progress in Aerospace Sciences, Volume 37, Issue 7, pp. 487-545, 2000.
2. Seifert, A. and Pack, L. G., "Active Flow Separation Control on Wall-Mounted Hump at High Reynolds Numbers," AIAA Journal, Vol. 40, No. 7, July 2002 (also see AIAA Paper 99-3403).
3. Seifert, A. and Pack, L.G., "Effects of Compressibility and Excitation Slot Location on Active Separation Control at High Reynolds Numbers", Journal of Aircraft Vol. 40, No. 1, pp. 110-119, Jan-Feb 2003.
4. Rumsey, C., Gatski, T., Sellers, W., Vatsa, V., Viken, S., "Summary of the 2004 CFD Validation Workshop on Synthetic Jets and Turbulent Separation Control", AIAA-2004-2217, 34th AIAA Fluid Dynamics Conference and Exhibit, Portland, Oregon, 28 June - 1 July 2004.
5. Greenblatt, D., Paschal, Yao, C., Harris, J., K., Schaeffler, N., and Washburn, A., "A separation control CFD validation test case. Part 1: Baseline & steady suction", AIAA Paper 2004-2220, 2nd AIAA Flow Control Conference, Portland, Oregon, 28 June - 1 July 2004.

6. Poisson-Quinton, Ph. and Lepage, L., "Survey of French research on the control of boundary layer and circulation", in Lachmann, G. V., "Boundary layer and Flow Control. Its Principles and Application", Vol. 1, pp. 21-73, Pergamon Press, New York, 1961.
7. Schlichting, H., "Boundary Layer Theory", McGraw-Hill, 1979.
8. Rumsey, C., "Private Communication", 2003-2004.
9. Batchelor, G. K. An Introduction to Fluid Dynamics. New York: Cambridge University Press, 1977.
10. Hussain, A.K.M.F. and Reynolds, W.C., "The Mechanics of an organized Wave in Turbulent Shear Flow", J. Fluid Mechanics, 41(1), part 2., 1970, pp. 241-258.
11. Reynolds, W.C and Hussain, A.K.M.F., "The Mechanics of an organized Wave in Turbulent Shear Flow. Part 3. Theoretical models and comparisons with experiments", J. Fluid Mechanics, 54, part 2., 1972, pp. 263-288.
12. Obi, S., Ishibashi, N. and Masuda, S. "The mechanism of momentum transfer enhancement in the periodically perturbed turbulent separated flow", 2nd Int. Symposium on Turbulence, Heat and Mass Transfer, ed. Hanjalić, K. and Peeters, T.W.J., Delft University Press, pp. 835-844, 1997.
13. Attinello, J. S. "Design and engineering features of flap blowing installations", in Lachmann, G. V., "Boundary layer and Flow Control. Its Principles and Application", Volume 1, pp. 463-515, Pergamon Press, New York, 1961.
14. Seifert, A., Darabi, A. and Wygnanski, I., "Delay of airfoil stall by periodic excitation", AIAA Journal of Aircraft, Vol. 33, No. 4, 1996, pp. 691-698.
15. Nishri, B. and Wygnanski, I. "Effects of periodic excitation on turbulent separation from a flap", AIAA Journal, Vol. 36, No. 4, 1998, pp. 547-556.
16. Ho, C. and Huerre, P., "Perturbed free shear layers", Annual Review of Fluid Mechanics, Vol. 16, pp. 365-422, January 1984.

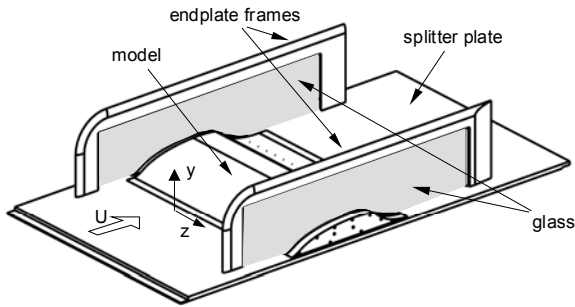


Fig. 1. Perspective view of the experimental setup, showing the model, endplates and splitter plate.

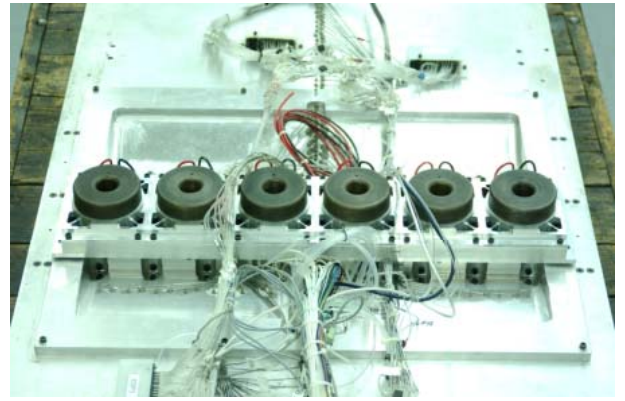


Fig. 4. Photograph of the actuators mounted on the underside of the model (model is inverted).

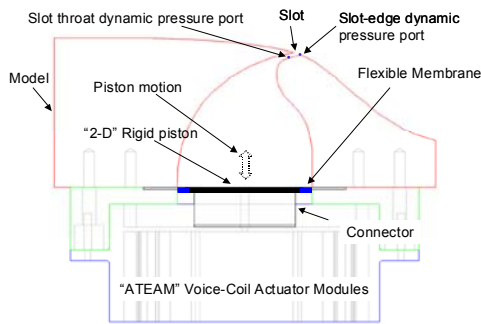


Fig. 2. Side-view schematic showing the voice-coil actuator and piston assembly.

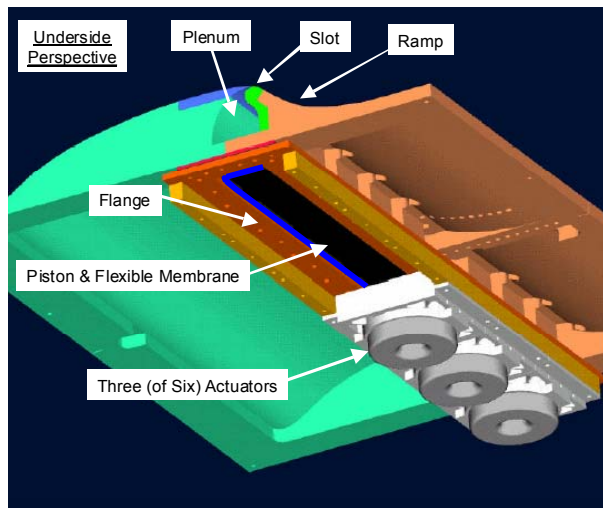


Fig. 3. Underside perspective of the hump model actuator assembly. Three of the six voice-coil actuators are removed for illustrative purposes.

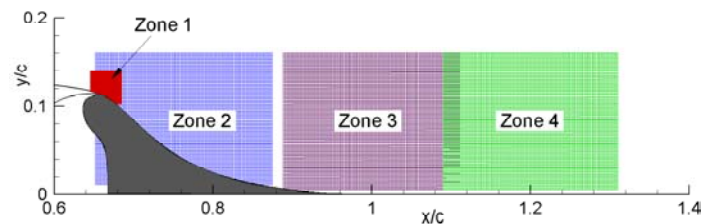


Fig. 5. Schematic of the ramp showing the four zones in which baseline and phase-resolved two-dimensional PIV measurements were acquired.

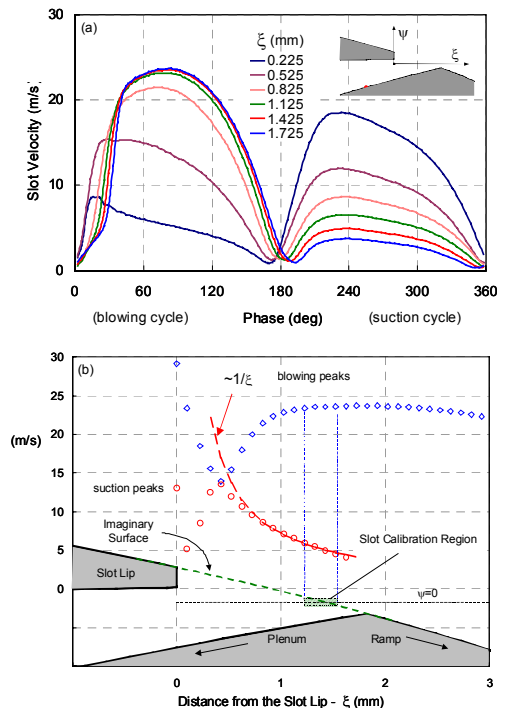
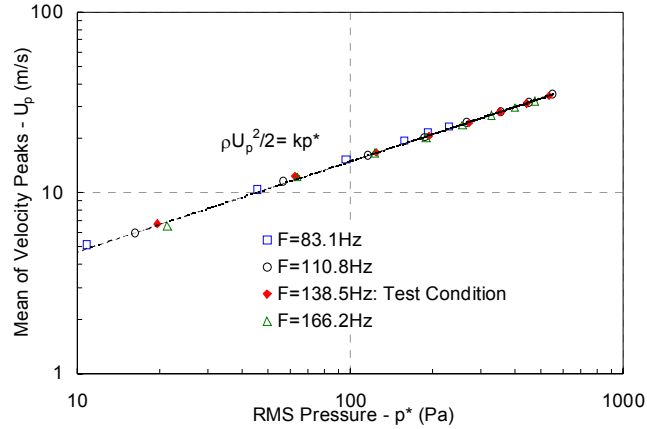
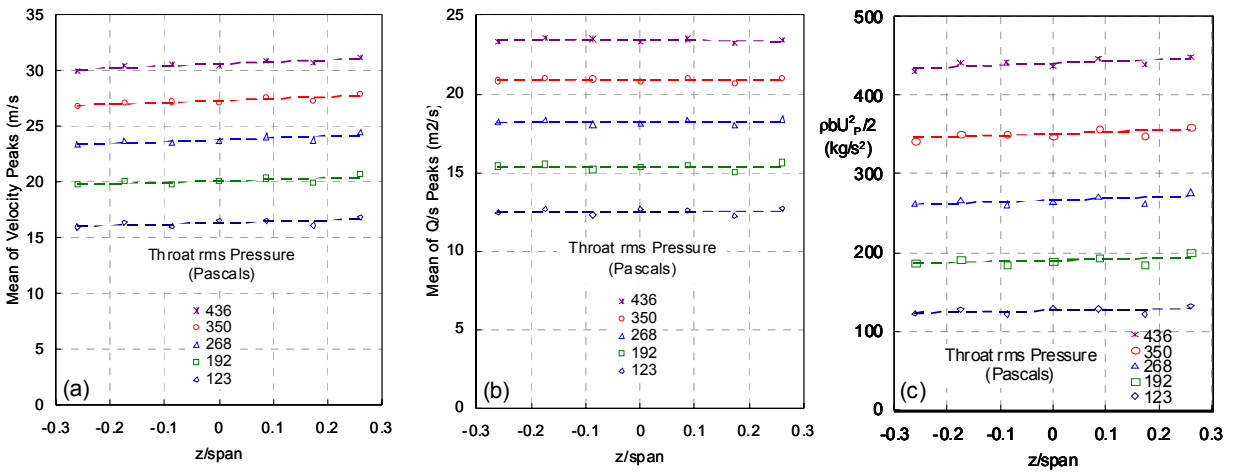


Fig. 6 (a) Hot-wire traces from within the slot traversing the imaginary line between the upper and lower edges of the slot. ( $\xi=0$  is measured from the slot upper edge;  $\psi=0$  is defined as half-way between the upper and lower slot edges); (b) phase-averaged blowing and suction peaks for  $\xi \geq 0$ .



**Fig. 7. Correlation of throat rms “deliver pressure” and phase-averaged peak blowing velocities.**



**Fig. 8. Spanwise measurements of phase-averaged (a) peak blowing velocities; (b) phase-averaged peak blowing mass-flux; and (c) peak momentum-flux.**

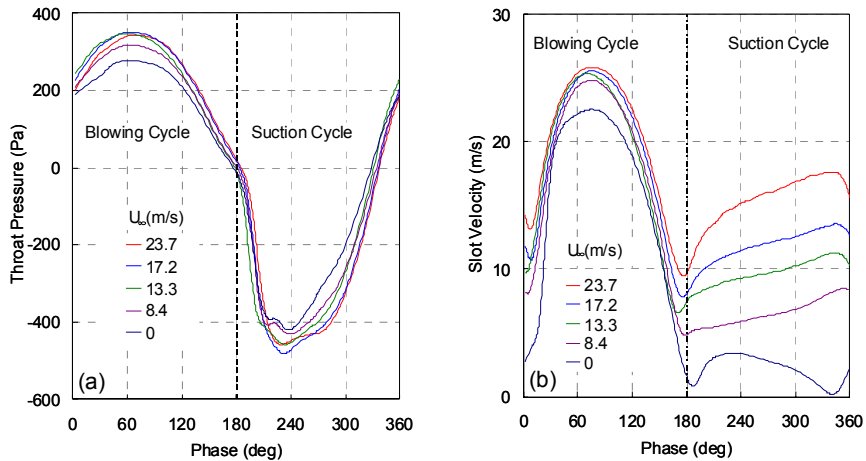


**Fig. 9. (a) Throat pressure traces and (b) hot-wire traces of slot velocities for zero and non-zero values of  $U_\infty$**

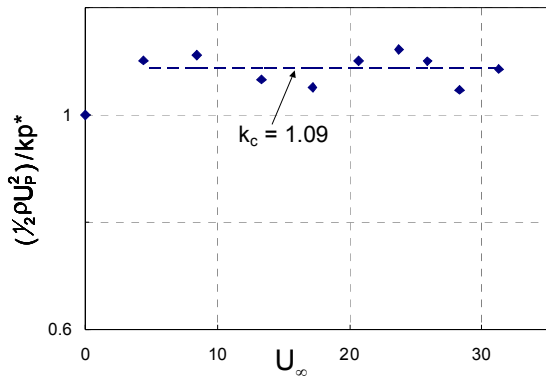


Fig. 10. Effect of non-zero free-stream velocity on slot jet calibration.

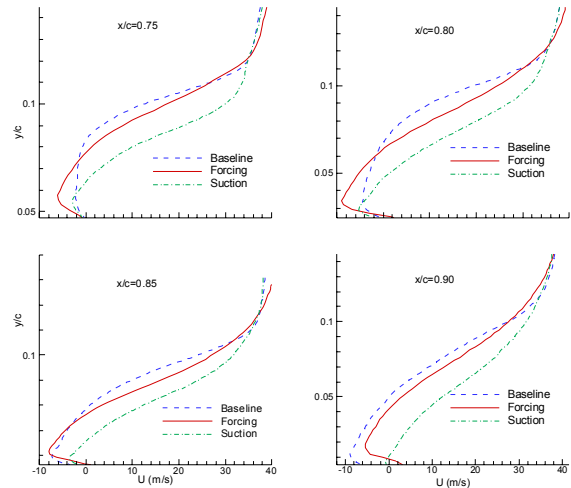


Fig. 12. Velocity profiles on the ramp corresponding to baseline and time-mean controlled scenarios.

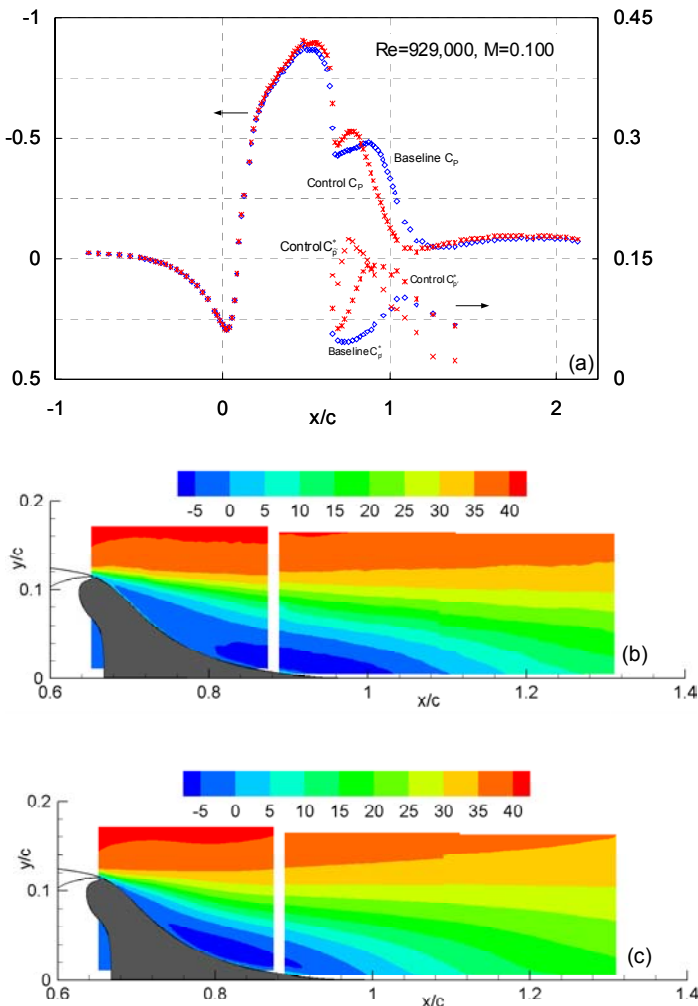


Fig. 11. (a) Baseline and controlled mean and fluctuating surface pressures on the model; (b) baseline streamwise velocity contours (in m/s) in the separated flow region; (c) controlled time-mean streamwise velocity contours (in m/s) in the separated flow region.

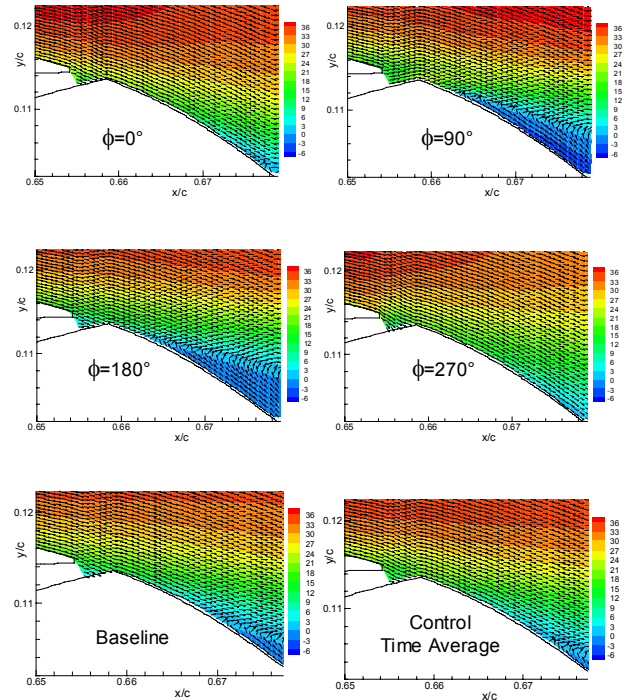


Fig. 13. Phase-averaged streamwise velocity contours (m/s) and normalized  $\langle u \rangle - \langle v \rangle$  vectors for indicating flow direction at four phases of the control cycle corresponding to zone 1 in fig. 5. Also, corresponding baseline and time-mean control data.

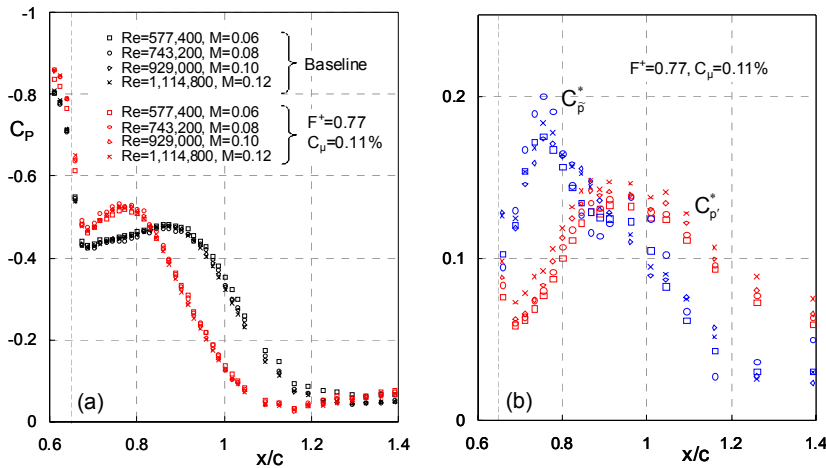


Fig. 14. Effect of Reynolds number on mean and fluctuating surface pressures (vertical line indicates slot location).

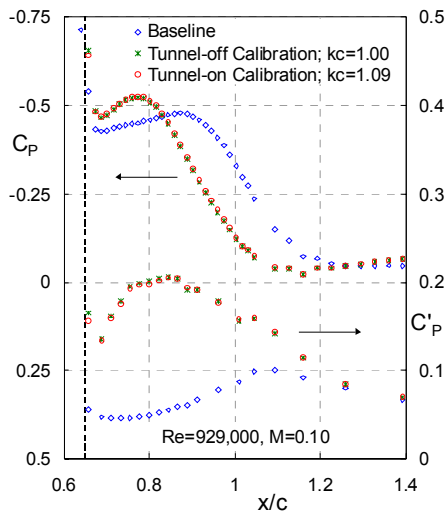


Fig. 15. Mean and fluctuating pressures based on quiescent and non-quiescent slot calibrations.

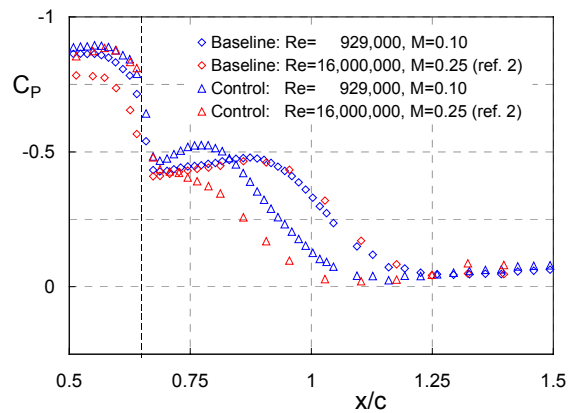


Fig. 16. Comparison of atmospheric and cryogenic data sets at the test case condition representing a factor of 16 difference in Reynolds number. Control at  $F^* = 0.77; C_{\mu} = 0.11\%$ .

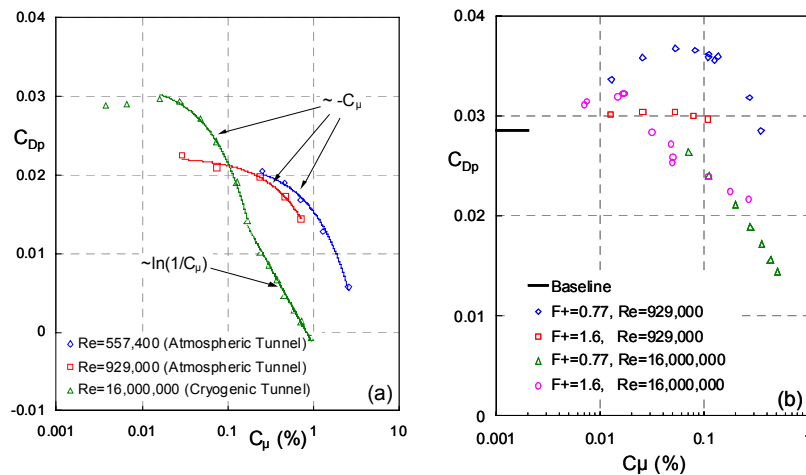


Fig. 17 (a) comparison of atmospheric and cryogenic data sets (ref. 2) for steady suction; (b) comparison of atmosphere and cryogenic data sets (ref. 2) for zero efflux control at different reduced frequencies.

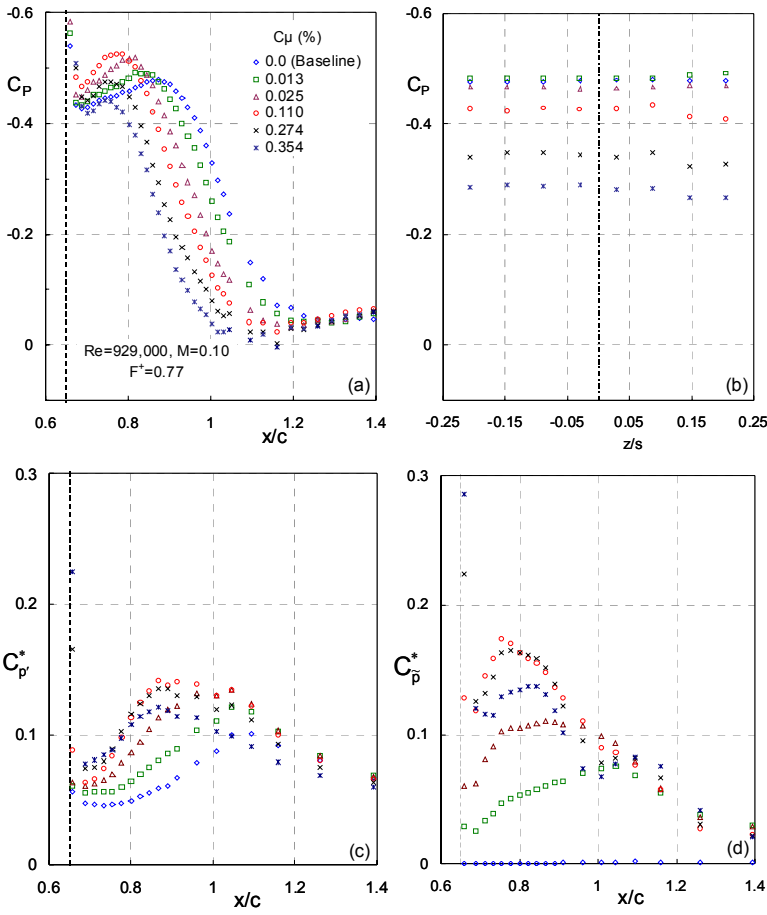


Fig. 18. (a) Mean streamwise; (b) mean spanwise; (c) turbulent rms; and (d) coherent rms pressure coefficients for various control amplitudes at the test case reduced frequency.

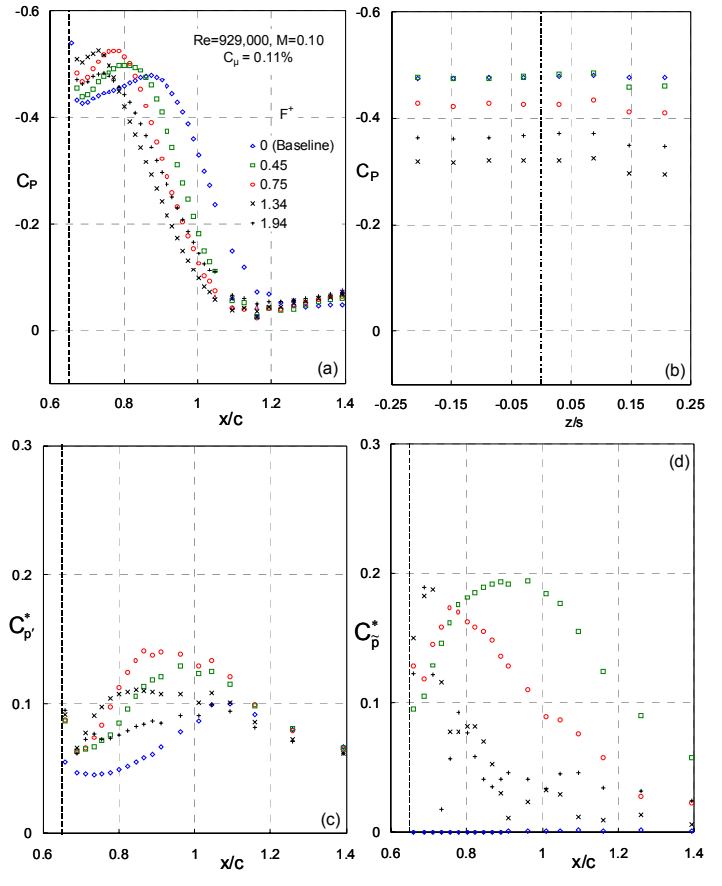


Fig. 19. (a) Mean streamwise; (b) mean spanwise; (c) turbulent rms; and (d) coherent rms pressure coefficients for various control frequencies at the test case reduced amplitude.

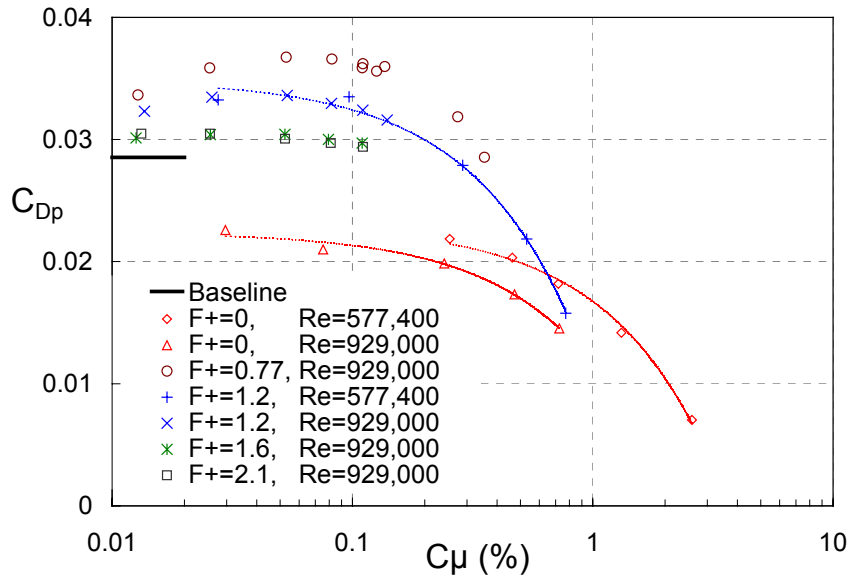
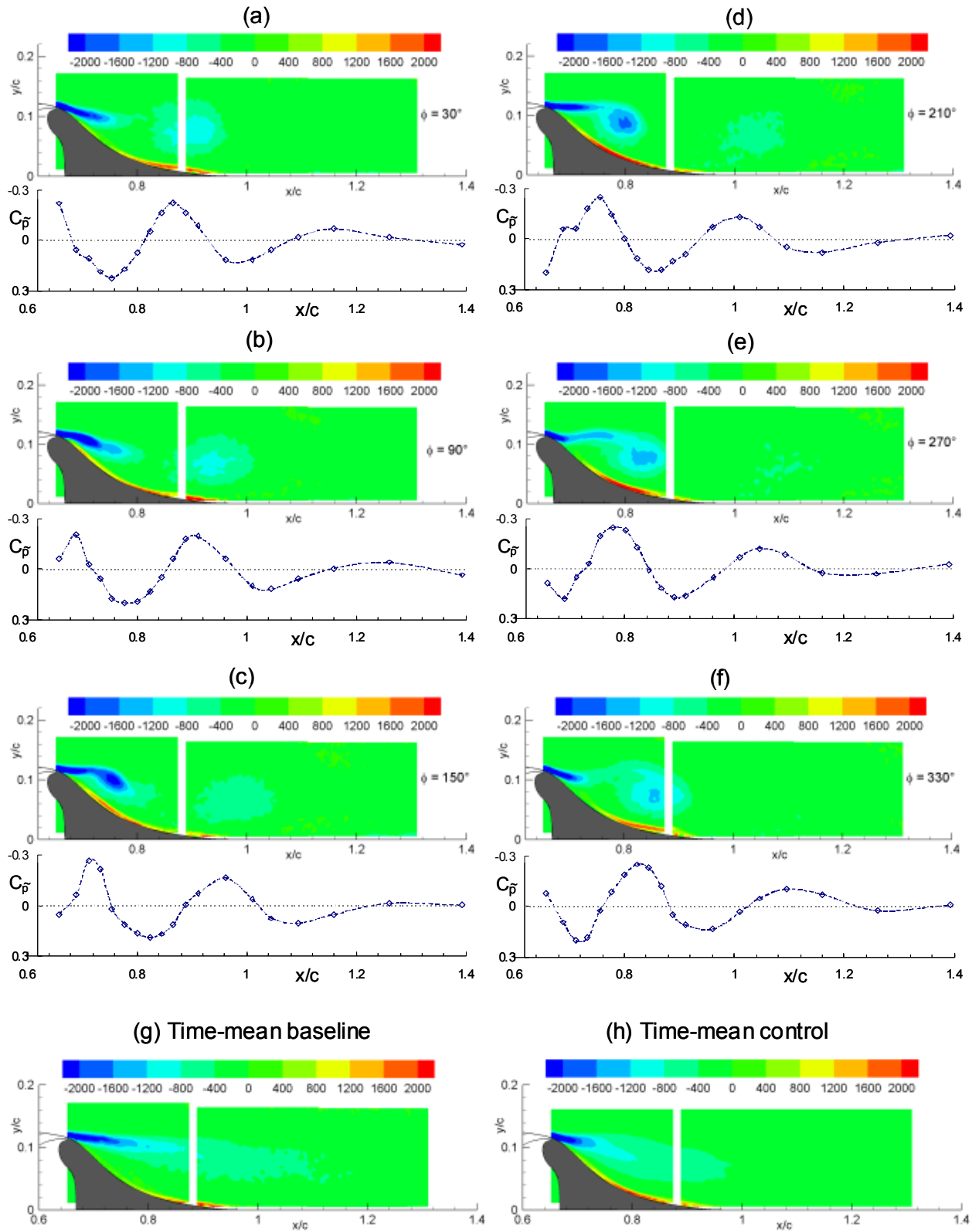


Fig. 20. A comparison of the form drag coefficient for zero efflux and steady suction on the basis of  $C_u$ .



**Fig. 21. (a-f) Phase-averaged spanwise vorticity field  $\langle \omega_z(x, y, t) \rangle$  with corresponding coherent surface pressure fluctuations  $C_{\tilde{p}} = \langle C_p \rangle - C_p$  at six phases of the control cycle; (g) baseline and (h) corresponding time-mean.**

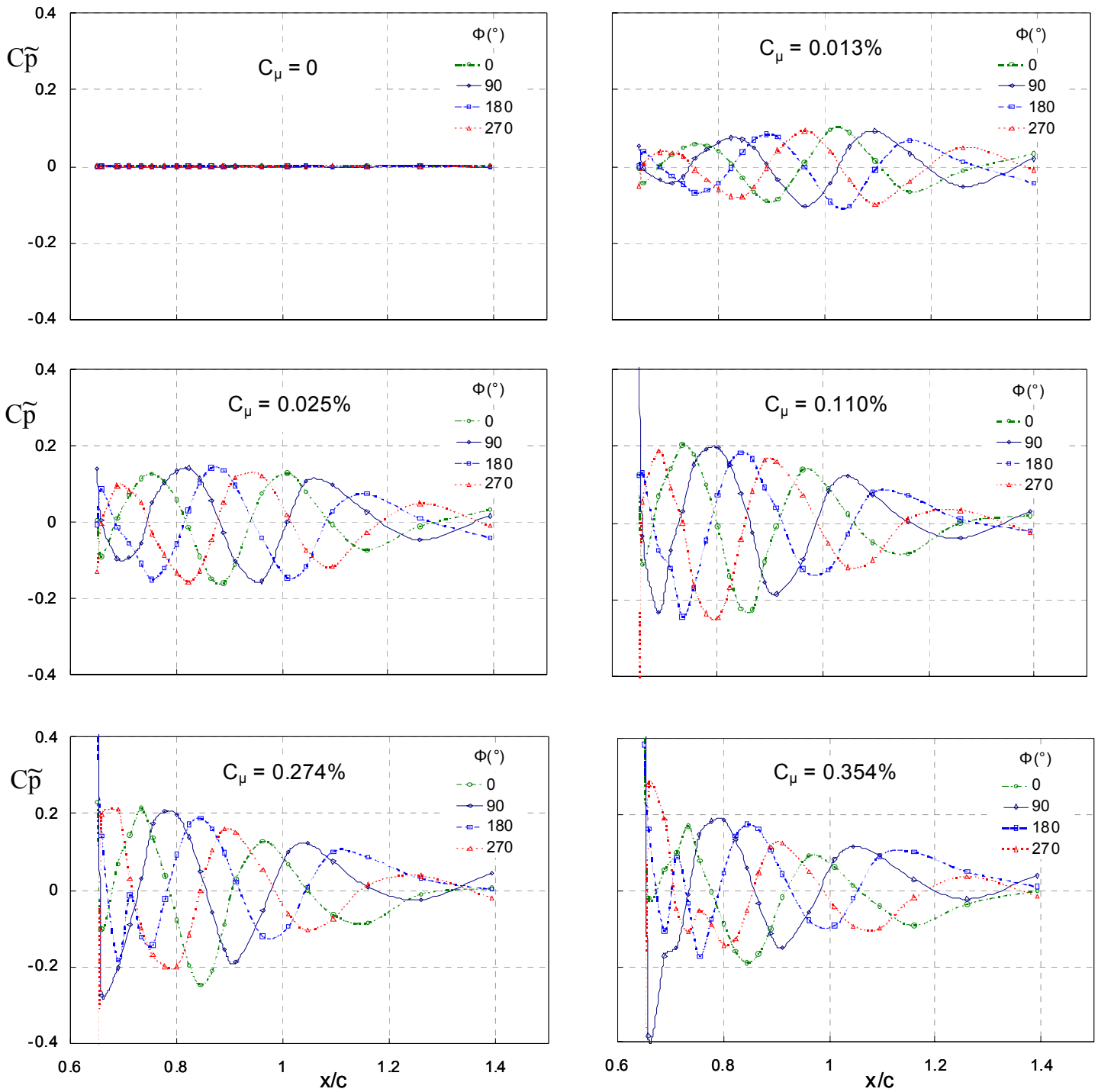


Fig. 22. Coherent surface pressure fluctuations  $C_{\tilde{p}}$  for various control amplitudes at the test case reduced frequency.

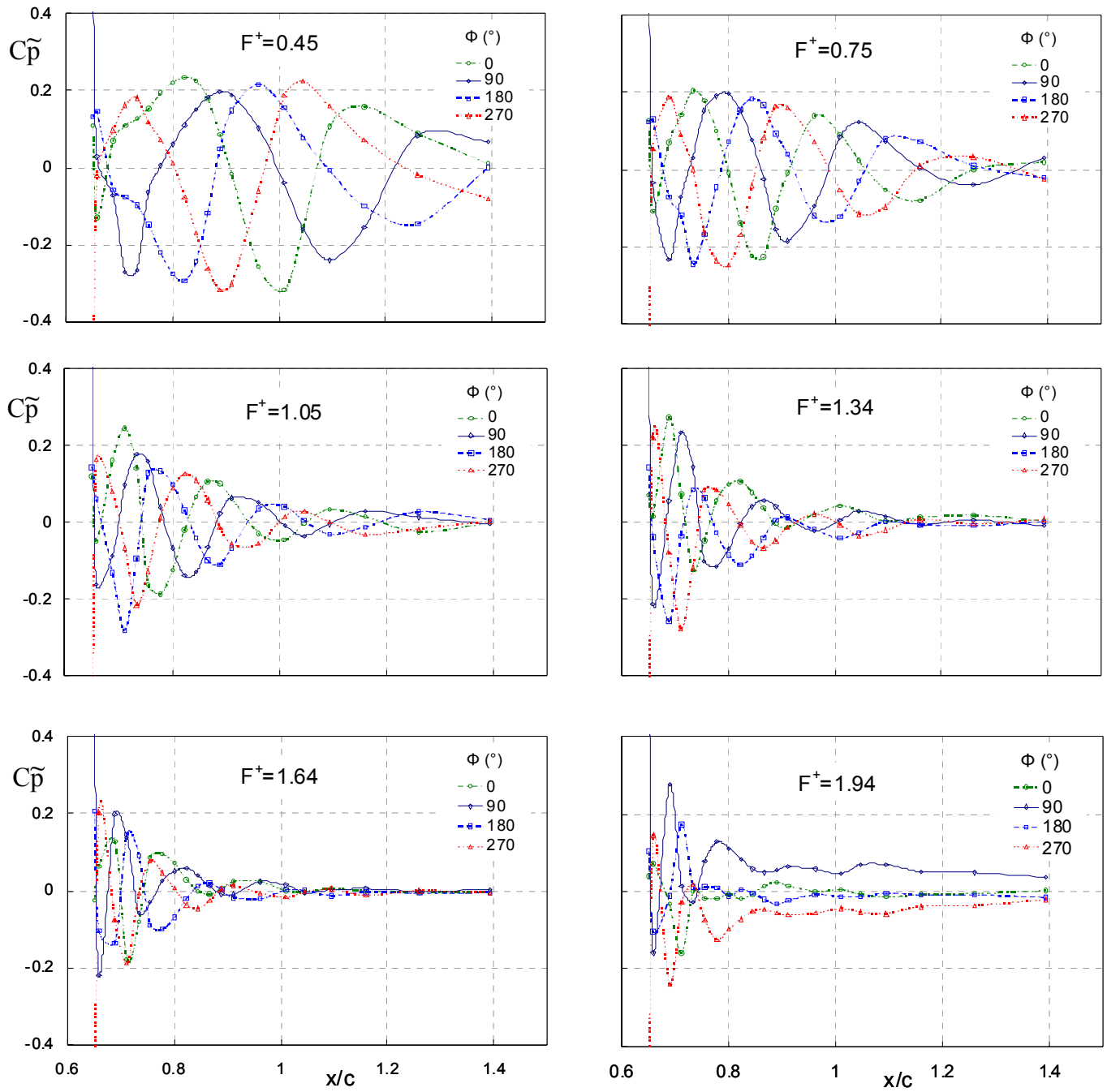


Fig. 23. Coherent surface pressure fluctuations  $C_{\tilde{p}}$  for various control frequencies at the test case reduced amplitude.

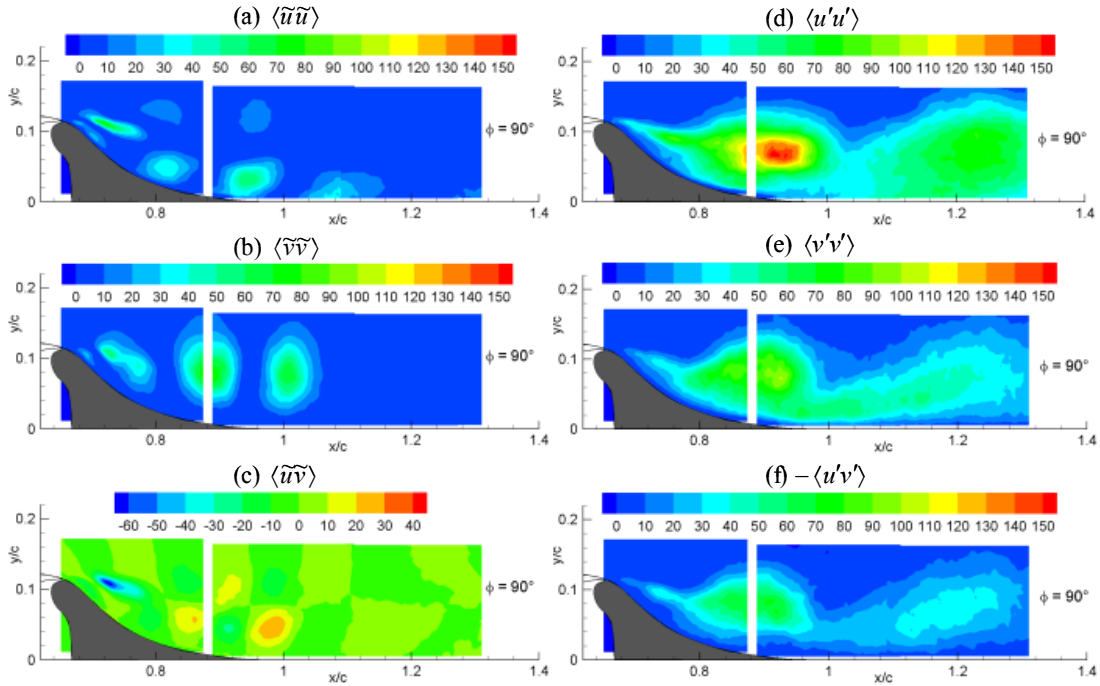


Fig. 24. Phase-averaged coherent and turbulent Reynolds stresses at  $\phi=90^\circ$  (all data in  $\text{m}^2/\text{s}^2$ ).

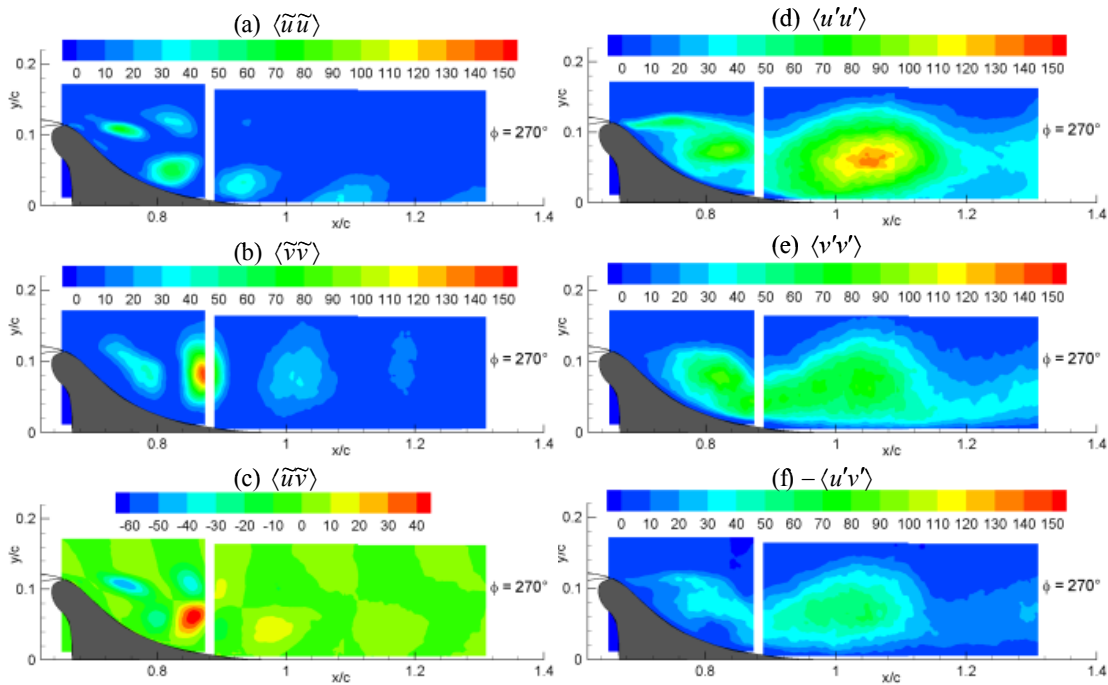


Fig. 25. Phase-averaged coherent and turbulent Reynolds stresses at  $\phi=270^\circ$  (all data in  $\text{m}^2/\text{s}^2$ ).

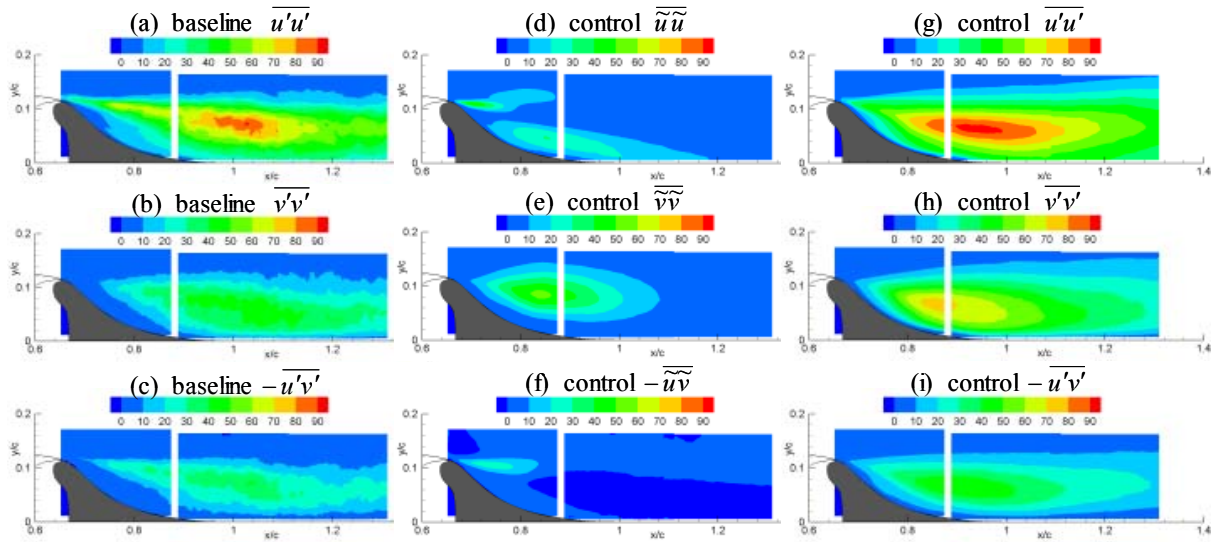


Fig. 26. Time mean baseline Reynolds stresses and time-mean coherent and turbulent Reynolds stresses (all data in  $\text{m}^2/\text{s}^2$ ).

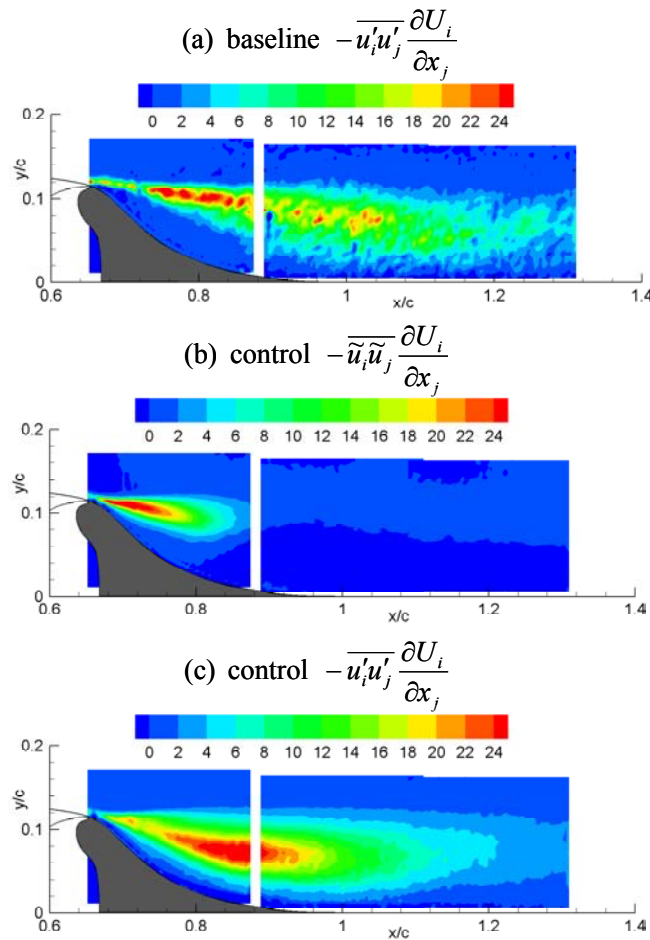


Fig. 27. Energy fluxes from the mean flow to the coherent and turbulent components (all data in  $\text{m}^2/\text{s}^3$ ).

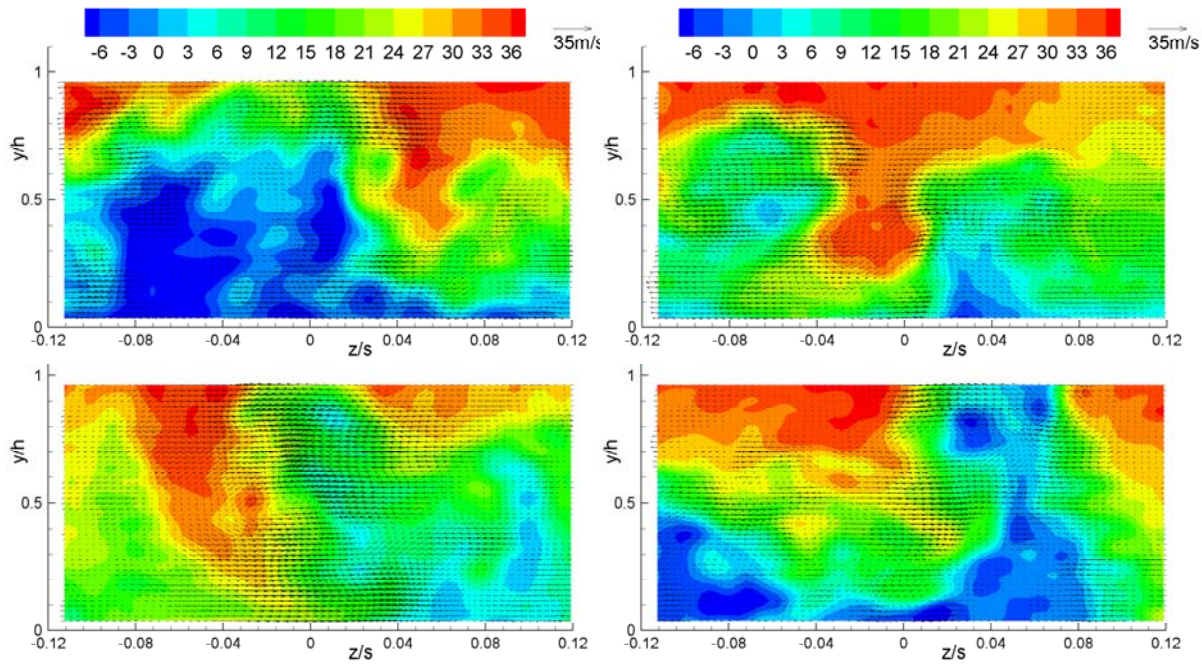


Fig. 28. Four examples of instantaneous velocities at  $x/c=1.0$  and  $\phi=60^\circ$ . Contours are the  $u$ -component; vectors are  $v$ - $w$  (all data in m/s).

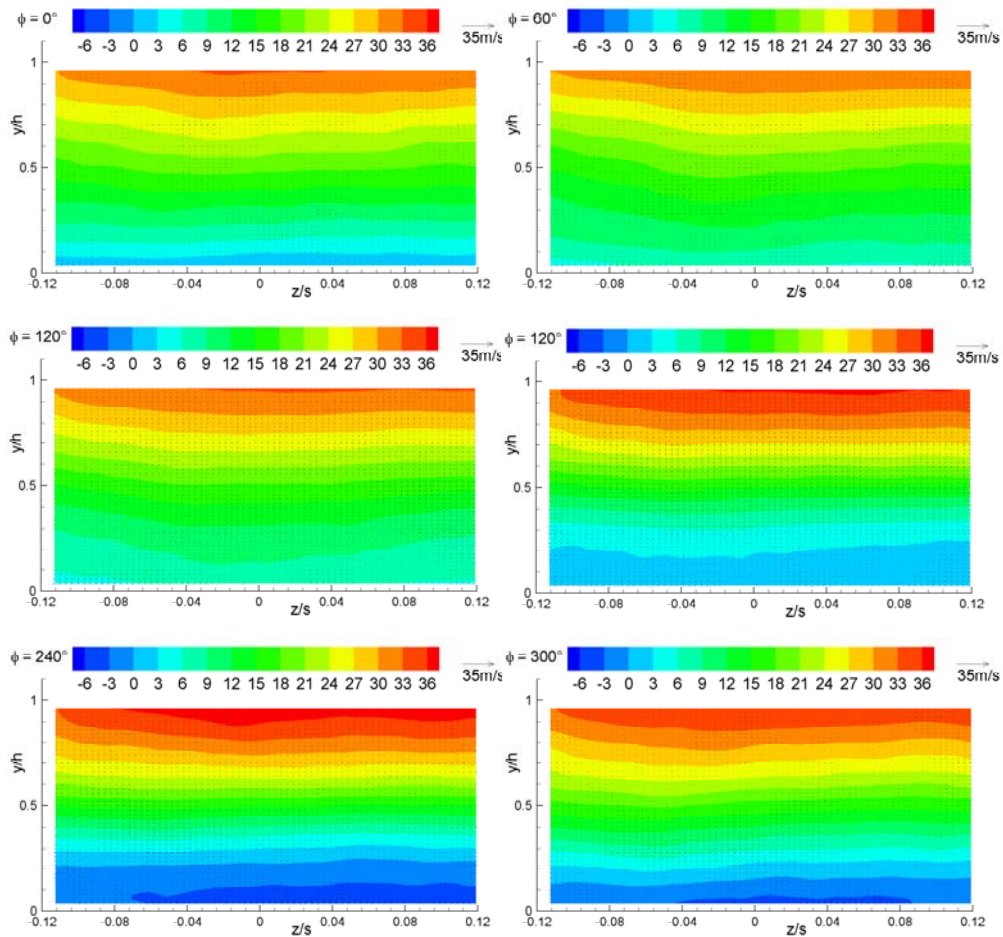


Fig. 29. Phase-averaged velocities for six phases at  $x/c=1.0$ . Contours are the  $u$ -component; vectors are  $v$ - $w$  (all data in m/s).

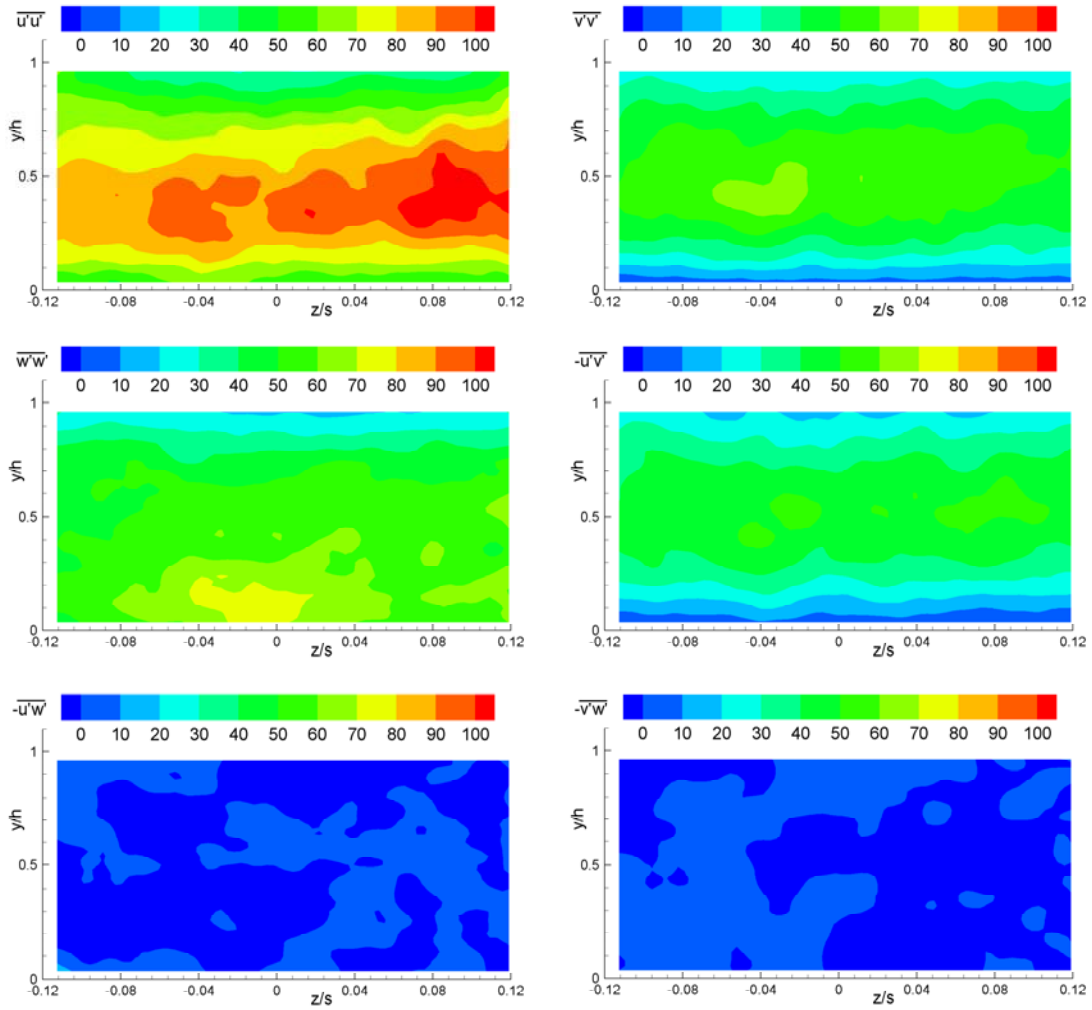


Fig. 30. Phase-averaged Reynolds stresses at  $x/c=1.0$  and  $\phi=0^\circ$  (all data in  $\text{m}^2/\text{s}^2$ ).